



## Reports from Research Areas

---

**Pictures on page 49** (from left to right):

Highly strengthened Cu-Ag tape

[Co/Pt]Ru, magnetic force microscopy images

Ni-Mn-Ga fibres

Part of the atomic structure of  $C_{60}(C_2H_4)_6$

## Research Area 1

### Superconductivity and superconductors

#### Remarkable physics of the “cushion” Fermi surface sheet in borocarbides

G. Fuchs, S.-L. Drechsler, H. Rosner, G. Behr, W. Löser, M. Schneider, K.-H. Müller, L. Schultz, H. Eschrig

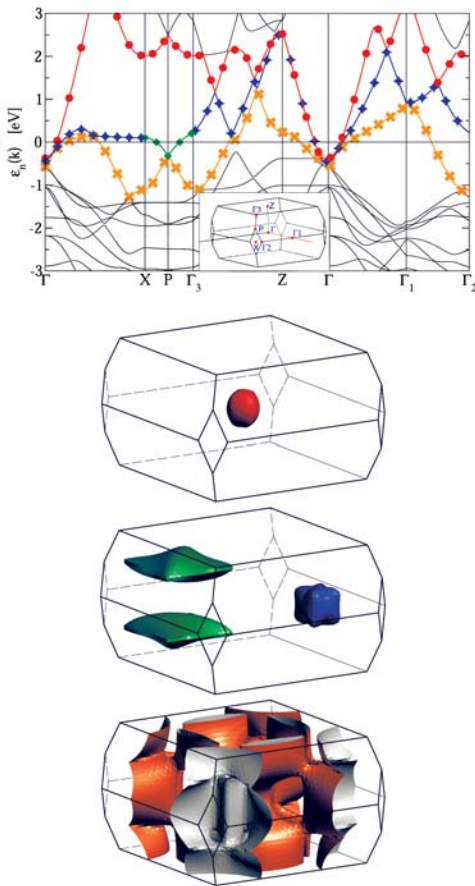


**Fig.:** Band structure and Fermi surface sheets (FSS) of  $\text{LuNi}_2\text{B}_2\text{C}$  within FPLO. “Green” FSS – cushion, “blue” FSS – cube.

Surprisingly, even more than 13 years after its discovery superconductivity and rare-earth magnetism in borocarbides  $R\text{Ni}_2\text{B}_2\text{C}$  continue to draw significant attention. This is caused by a nontrivial interplay of many-body interactions on their complex Fermi surface (Fig.) and results in not yet fully understood multi-band behavior, anisotropic superconducting gaps for  $R=\text{Y}, \text{Lu}, \text{Sc}$ , and rich magnetic phase diagrams including sometimes also unusual quadrupolar phases for  $R=\text{Ho}, \text{Dy}, \text{Er}, \text{Tm}$  etc.. Under these circumstances, it is important to have an emerging electronic feature common to all these compounds: a pure Ni  $3d$  state-derived “cushion” Fermi surface sheet (CFSS – Fig.) for which we obtained a growing number of related physical properties.

For  $R=\text{Ho}, \text{Dy}$ , the CFSS provides a place where in clean samples superconductivity may easily coexist with commensurate  $c$ -axis antiferromagnetism. The energy gap  $\Delta(T)$ , and a characteristic phonon mode near 10 meV derived from point contact spectra result in a local electron-phonon coupling constant  $\lambda \approx 0.9$  within a single-band Eliashberg picture [1] in accord with the upper critical field  $H_{c2}(0)$  and the average Fermi velocity of  $2.1 \times 10^5$  m/s predicted as  $1.9 \times 10^5$  m/s within the highly precise full-potential local-orbital (FPLO) band structure code. A similar coupling constant  $\lambda \approx 1$  has been found in de Haas-van-Alphen (dHvA) measurements for  $R=\text{Lu}$  by comparing observed orbital masses with their bare masses calculated by the FPLO code [2].

In the more complex multi-band nonmagnetic borocarbides the CFSS is *not* dominant for superconductivity. Much higher  $\lambda$  values up to 3 were observed for the cube FSS in Fig., although, with a low partial density of states, whereas other dHvA frequencies could not be assigned so far. In this sense, the electrons responsible for the relative high  $T_c \approx 15 - 16$  K and the large jump of the specific heat at  $T_c$  remain unknown. Anyhow, we believe that based on the achieved progress and further intensive dialogs between experiment and theory, a fully self-consistent picture will emerge in near future and the remaining puzzles can be finally resolved.

[1] Y.G. Naidyuk et al. Phys. Rev. B **76** (2007) 014520.

[2] B. Bergk et al. Phys. Rev. Lett. submitted.

**Cooperation** TU Dresden, MPI-CPFS, HLD Rossendorf, Inst. f. Low-Temperature Physics and Engineering, Kharkov, Ukraine, Ames Laboratory, Iowa, USA, Grenoble High-Field Lab. CNRS, France.

**Funded by** DFG (SFB 463, Emmy-Noether-Program)

#### Momentum and excitation energy dependence of the anomalous high-energy dispersion in cuprates

D. S. Inosov, J. Fink, A. Kordyuk, S. V. Borisenko, V. B. Zabolotny, R. Schuster, M. Knupfer, B. Büchner

It is widely believed that the study of many-body effects in the electronic structure of layered cuprates is a possible clue to the mechanism of high-temperature superconductivity in these materials. However, even after years of intense studies there is still no full understanding of the renormalization effects and of the relevant energy scales in their electronic excitation spectrum. Recently there was a series of publications evidencing

anomalous high-energy dispersion in the renormalized band structure of cuprates at the binding energies higher than 0.3–0.5 eV — a region that has previously been scarcely explored. Using high-resolution angle-resolved photoemission spectroscopy we have studied the momentum and photon energy dependence of this anomalous high-energy dispersion, termed “waterfalls”, between the Fermi level and 1 eV binding energy in several high- $T_c$  superconductors. We observe strong changes of the dispersion between different Brillouin zones and a strong dependence on the photon energy around 75 eV (see figure), which we associate with the resonant photoemission at the Cu 3p3d  $x^2-y^2$  edge. We conclude that the high-energy “waterfall” dispersion results from a strong suppression of the photoemission intensity at the center of the Brillouin zone due to matrix element effects and is, therefore, not an intrinsic feature of the spectral function. This indicates that the postulated new high-energy scale in cuprates near 0.4 eV is not inherent in the single-particle spectral function of these materials. At least we emphasize that due to matrix element effects this new energy scale can be hugely distorted, complicating correct determination of the real dispersion, which is crucial for the high- $T_c$  superconductivity problem, where understanding the nature of coupling requires the knowledge of very fine details of both the one-particle and two-particle spectra.

**Cooperation** BESSY GmbH, Berlin, Germany; MPI for Solid State Research, Stuttgart, Germany; Institut de Physique de la Matière Complexe, Lausanne, Switzerland  
**Funded by** DFG

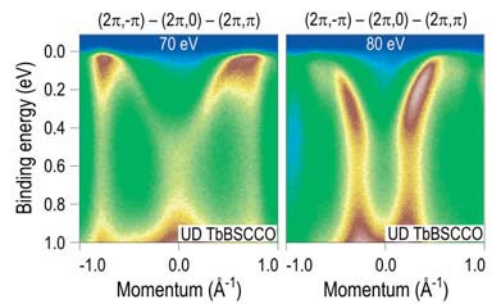
### Scanning Tunneling Microscopy on underdoped $\text{YBa}_2\text{Cu}_3\text{O}_{7-\delta}$

G. Urbanik, T. Hänke, C. Hess, B. Büchner, A. Ciszewski (1), V. Hinkov (2), C.T. Lin (2), B. Keimer (2)

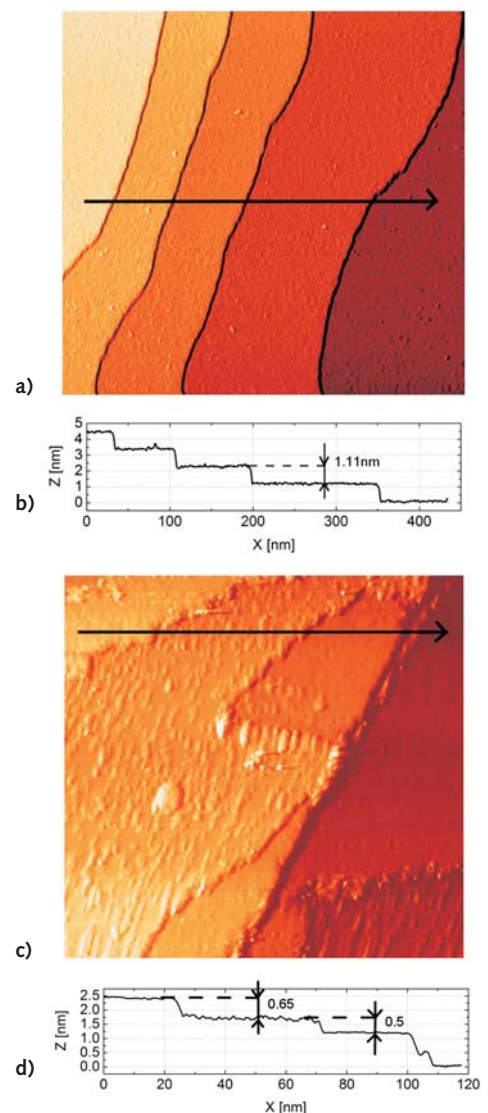
We performed a Scanning Tunneling Microscopy (STM) surface study on high quality detwinned underdoped  $\text{YBa}_2\text{Cu}_3\text{O}_{6.6}$  crystals which were cleaved at low temperature (<40 K) under Ultra-High-Vacuum (UHV) conditions. Our investigations reveal that at this doping level the surface obtained upon cleaving clearly differs from that of  $\text{YBa}_2\text{Cu}_3\text{O}_{7-\delta}$  close to optimal doping. For the latter case cleaving at low temperature and in UHV has been reported to mainly lead to either BaO or CuO (chain) sheets as the topmost layer. In our study for the doping level  $\delta=0.4$  we find that in most instances (95%) only one type of termination is exposed. This type of surface usually exhibits a high corrugation ( $\sim 3 \text{ \AA}$ ) and adjacent surfaces are separated by steps with a height  $\Delta_z \approx 1.1 \text{ \AA}$ , which corresponds to the c-lattice constant of the compound (see figure). Combined with the symmetry of the crystal lattice this implies that cleaving takes place at either the CuO chain layer or the Y-layer involving a redistribution of the layer atoms on the two cleaved surfaces. Taking into account that at this doping level the oxygen deficiency leads to a high number of broken chain structures in the CuO chain layer we conclude that the majority of cleaving events take place at these layers involving a disruption of the CuO layers. In rare cases ( $\sim 5\%$  abundance) we observed steps with a fractional step height  $\Delta_z \approx c/2$  (see figure), which indicates that cleaving at the Y-layer is also possible but less frequent.

**Cooperations** Univ. of Wrocław, Poland (1), MPI für Festkörperforschung, Stuttgart (2)  
**Funded by** Klaus Tschira Stiftung

**Fig.:** a) STM topographic image (500 nm  $\times$  500 nm) of the cleaved surface of  $\text{YBa}_2\text{Cu}_3\text{O}_{6.6}$  at 25 K obtained with a sample bias voltage  $V_{\text{bias}} = -1.5 \text{ V}$  and tunneling current  $I_t = 0.1 \text{ nA}$ . Flat terraces and steps with the height  $\Delta_z \approx 1.1 \text{ nm}$  are visible. b) Line profile from a). c) Topographic image (125 nm  $\times$  125 nm) showing different types of termination layers. The typical detected step height differences are  $\Delta_z \approx 0.65 \text{ nm}$  and  $\Delta_z \approx 0.5 \text{ nm}$ . The most common layer has higher corrugation. d) Line profile from c).



**Fig.:** A pair of equivalent spectra of Tb-doped Bi-2212 taken in the 2<sup>nd</sup> Brillouin zone along the  $(\pi; 0)$  and  $(\pi; \pi)$  directions with two different excitation energies as indicated on top of each panel. The color scale represents photoelectron intensity. The onset of the “waterfalls” behavior suddenly occurs at about 75 eV photon energy, below which a Y-shaped dispersion is observed.



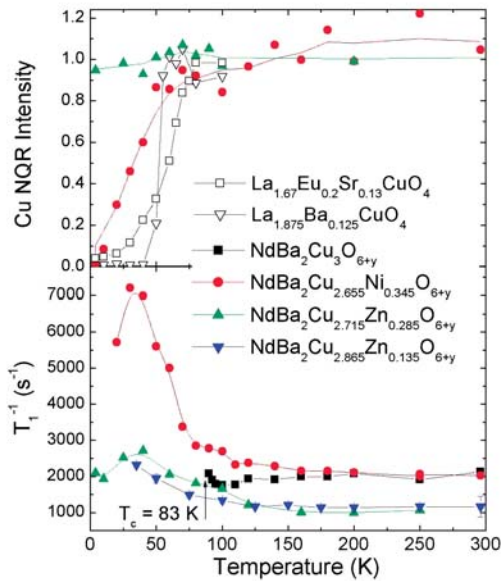


Fig.: Upper panel: Cu NQR signal intensity for Ni and Zn doped NBCO in comparison to stripe ordered lanthanum cuprates. Ni induces a wipeout of the signal intensity. Lower panel: Cu spin lattice relaxation rate,  $T_1^{-1}$ , for Zn and Ni doped NBCO. Ni enhances  $T_1^{-1}$ , while Zn doping reduces  $T_1^{-1}$  even at high temperatures.

## Cu NQR Wipeout Effect and Charge Pseudogap in Zn/Ni doped $\text{NdBa}_2(\text{Cu,Zn,Ni})_3\text{O}_{6+y}$

H.-J. Grafe, F. Hammerath, A. Vyalikh, G. Urbanik, V. Kataev, B. Büchner

Magnetic (Ni) as well as non-magnetic (Zn) substitution for copper in high temperature superconductors (HTSC) reduces the superconducting transition temperature,  $T_c$ , quite rapidly. Moreover, Ni and Zn doping affects also the unusual normal state electronic properties of HTSCs. It has been observed that a  $S=0$  Zn impurity induces magnetic moments on the neighboring Cu sites in underdoped cuprates [1,2]. Recently it was found that higher amounts of Ni and Zn can be incorporated in  $\text{NdBa}_2\text{Cu}_3\text{O}_{6+y}$ , and thereby superconductivity is fully suppressed even at optimal doping [3]. Measurements of the optical conductivity that probes the *charge* excitations in these compounds show that Ni and Zn have a profoundly different impact on the pseudogap [3]. Large Zn-doping suppresses the pseudogap, whereas Ni enhances its energy scale. Therefore we have investigated the *spin* dynamics by means of nuclear quadrupole resonance (NQR) measurements on the Cu nucleus [4]. We find that Ni doping enhances the nuclear spin lattice relaxation rate,  $T_1^{-1}$ , while Zn reduces  $T_1^{-1}$  (see figure). Since  $T_1^{-1}$  probes the low frequency dynamic spin susceptibility of the  $\text{CuO}_2$  planes at the antiferromagnetic wave vector,  $\mathbf{Q}_{\text{af}}$ , we conclude that Ni enhances the antiferromagnetism, and thereby the hole localization and the charge pseudogap. In contrast, large amounts of Zn dilute the spin system, and thus the low energy spin collective modes are suppressed. The fast spin lattice relaxation as observed for the Ni doped sample leads to a wipeout of the Cu signal intensity at low temperatures. Such a wipeout has been observed in the stripe ordered lanthanum cuprates, too [5]. The wipeout confirms our conclusion that the Ni doping enhances the antiferromagnetism and thereby the hole localization.

[1] H. Alloul *et al.*, Phys. Rev. Lett. **67**, 3140 (1990)

[2] M.-H. Julien *et al.*, Phys. Rev. Lett. **84**, 3422 (2000)

[3] A. V. Pimenov *et al.*, Phys. Rev. Lett. **94**, 227003 (2005)

[4] H.-J. Grafe *et al.*, submitted to Phys. Rev. B, arXiv:0705.3526

[5] N. Curro *et al.*, Phys. Rev. Lett. **85**, 642 (2000)

Cooperation FZ Karlsruhe, Germany; MPI Festkörperforschung, Stuttgart, Germany  
Funded by DFG, Forschergruppe 538

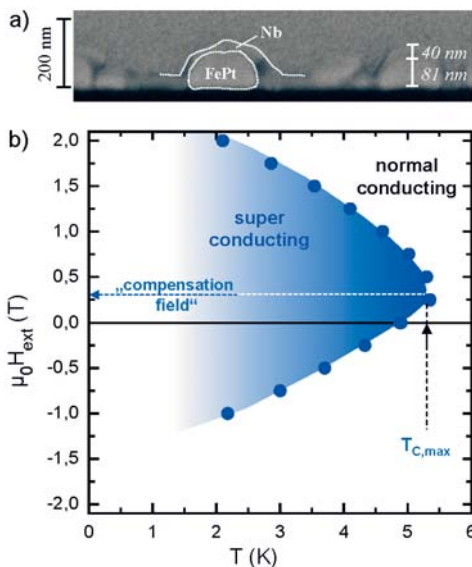


Fig.: a) Cross section of a Nb/FePt hybrid. b) Shift of the phase boundary due to stray field compensation effects.

## Highly coercive Superconducting/Ferromagnetic Heterostructures prepared by Pulsed Laser Deposition

S. Haindl, M. Weisheit, T. Thersleff, V. Neu, B. Holzapfel, L. Schultz

A ferromagnet in contact with a superconductor promises new physical effects. The spectrum of fields of interest ranges from the oscillation of the order parameter at the interface which causes oscillations in superconductive properties to the interaction of the vortices with magnetic domains and/or domain walls.

Artificial heterostructures composed of magnetic and superconducting materials offer the possibility to study the influence of magnetism on superconductivity experimentally. The effect of stray field compensation was discussed for Nb/FePt bilayers: The stray field of magnetic dots enters the superconductor; opposing to the stray field, an applied magnetic field is able to rise the superconductive transition temperature. So far only magnetic materials with a small coercivity have been employed.

In our recent experiments highly coercive materials, like  $\text{L}_{10}$  FePt and  $\text{SmCo}_5$ , have been combined with a conventional superconductor like Nb using UHV Pulsed Laser Deposition (PLD). On the one hand the epitaxial relation of Nb/ $\text{SmCo}_5$  multilayers has been

characterized by X-ray analysis and Transmission Electron Microscopy (TEM). On the other hand the island growth of FePt on MgO(100) single crystal substrates is an easy route for the fabrication of magnetic dots.

In Nb/FePt bilayers (figure *a*) an enhanced field compensation effect was found compared to similar heterostructures employing soft magnetic dots: An increase of the superconducting transition temperature of about 0.5 K was found when a magnetic field of 0.25 T was applied. The phase boundary of the superconductor in the B(T)-diagram was determined (figure *b*). In addition, within a sample series the variable FePt thickness shows a qualitative influence on the shape of the phase boundary. A successful combination of superconductors and highly coercive magnets has hereby been demonstrated.

Acknowledgment: Kerstin Hennig, Fritz Kurth

**Cooperation** TU Dresden

**Funded by** SFB 463/A4

## Research Area 2

### Magnetism and magnetic materials

#### Multidomain states in magnetic superlattices

U. K. Rößler, N. S. Kiselev, I. E. Dragunov, C. Bran, U. Wolff, V. Neu, A. N. Bogdanov

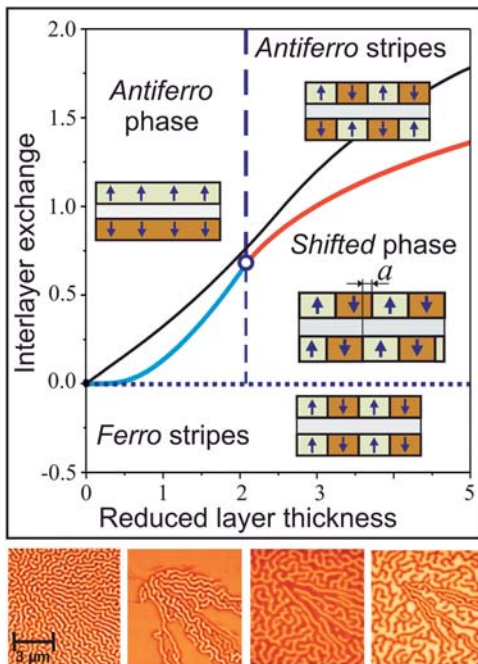


**Fig.:** Magnetic ground-state phase diagram for antiferromagnetically coupled bilayers with strong perpendicular anisotropy. The magnetic force microscopy images (bottom panel) from a [Co/Pt]Ru multilayer represent different possible domain configurations at the phase boundary between ferro stripes and antiferro phase.

Antiferromagnetically coupled multilayers with strong perpendicular magnetic anisotropy such as [Co/Pt]/Ru, [Co/Pt]/NiO, Co/Ir, Fe/Au represent a new class of magnetic materials with unique properties. These magnetic media are attractive for application in data storage technologies [1]. In such *synthetic metamagnets*, there is a wide variability of magnetic field-driven reorientation transitions and accompanying multidomain states. Within a micromagnetic theory we have classified and analysed the magnetic states of such multilayer structures [2]. A modified approach has been developed to derive analytical expressions for the existence regions and geometrical parameters of equilibrium stripe domains and their evolution in a bias field. In multilayers with ferromagnetic exchange coupling the equilibrium stripe widths can vary in broad ranges depending on relative values of the magnetic layer and spacer thicknesses. In superlattices with antiferromagnetic exchange coupling, three different ground states are realized: the homogeneous antiferromagnetic state and multidomain antiferromagnetic or ferromagnetic stripes. This ground-state phase structure is represented by phase diagrams in dependence on interlayer exchange coupling, thickness of the ferromagnetic single layer, and the number of layers. Our analytical approach enables simple calculations of stray fields emanating from such complex domain patterns. The method has been used to model the signal captured by a magnetic force microscope from this novel class of nanomagnetic systems [3].

[1] O. Hellwig et al., *J. Magn. Magn. Mater.* **319**, 13 (2007).

[2] N. S. Kiselev et al., *Appl. Phys. Lett.* **91**, 132507 (2007).

[3] N.S. Kiselev et al., *J. Appl. Phys.* in press.

**Cooperation** Hitachi Global Storage Technologies, San Jose Research Center, USA; Donetsk Institute for Physics and Technology, Ukraine

**Funded by** DFG (SPP1239, A8)

#### Magnetism of Pd overlayers

S. Schönecker, M. D. Kuzmin, M. Richter, K. Koepfner, H. Eschrig

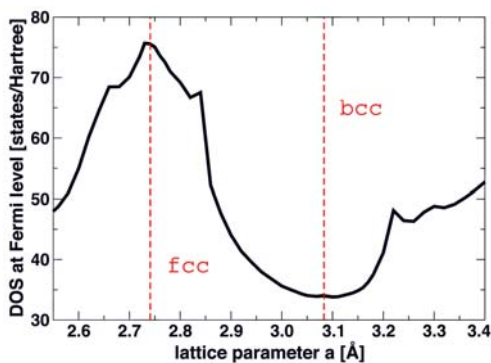


**Fig.:** Density of states at the Fermi level of Palladium along the tetragonal epitaxial Bain path. The *fcc* ground state exhibits the highest DOS at  $E_F$ . Broken red lines indicate the  $a$  values where  $c = \sqrt{2} \cdot a$  (*fcc*) and  $c = a$  (*bcc*), respectively.

Palladium is the elemental metal with the highest exchange-enhanced Pauli susceptibility [1]. It has early been predicted to undergo a metamagnetic phase transition [2], but no sign of any field-dependence has been detected in its high-field susceptibility up to 16 T [3]. Another route to magnetism might be the application of negative strain [4], e.g., by hetero-epitaxy on a substrate with a larger lattice constant. The mismatch will be partly compensated by relaxation perpendicular to the surface, but a net atomic volume enhancement in comparison to bulk Pd is expected. The related narrowing of the 4d-band might yield a larger density of states (DOS) at Fermi level ( $E_F$ ) and in turn the Stoner criterion for magnetic order might be fulfilled.

We checked this idea by local density approximation calculations using the FPLO code for tetragonally distorted Pd along the so-called epitaxial Bain path [5]. Along this path in lattice parameter space, the parameter  $a$  is assumed fixed by the substrate and the parameter  $c$  is relaxed to yield the minimum total energy. In this way, bulk-like overlayers are modelled with a geometry determined by the substrate while neglecting the electronic effect of substrate and interface.

The resulting DOS at  $E_F$  is shown in the Figure: It is maximum for the undistorted *fcc* structure of Pd. Any change of the parameter  $a$  results in a reduction of the DOS at  $E_F$  and, as a consequence, of the Pauli susceptibility. We hence can exclude the possibility of growing ferromagnetic Pd overlayers in a tetragonal structure if the electronic effect of the substrate can be neglected.

- [1] J.F. Janak, Phys. Rev. B **16** (1977) 255.  
 [2] E.P. Wohlfarth and P. Rhodes, Phil. Mag. **7** (1962) 1817; T. Jarlborg and A. J. Freeman, Phys. Rev. B **23** (1981) 3577.  
 [3] S. Foner et al., J. Appl. Phys. **39** (1968) 551.  
 [4] H. Chen et al., Phys. Rev. B **40** (1989) 1443.  
 [5] P. M. Marcus et al., Phys. Rev. B **66** (2002) 064111.

Funded by DFG, FOR 520

### Crystal growth and unusual spin dynamics of Ca-doped SrCuO<sub>2</sub>

F. Hammerath, H.-J. Grafe, A. Wolter, V. Kataev, P. Ribeiro, G. Behr, N. Hlubek, C. Hess, B. Büchner

High quality single crystals of SrCuO<sub>2</sub> have been grown with the travelling solvent floating zone (TSFZ) technique. The crystal structure of this compound contains one dimensional CuO<sub>2</sub> double chains as shown in the inset of the figure. The Cu-spins ( $S=1/2$ ) of each chain couple antiferromagnetically, while the coupling between the chains is frustrated and hence can be neglected. Since the discovery of high temperature superconductors, low dimensional copper oxide compounds have gained a lot of interest not only due to their similarities to the high  $T_c$  compounds, but also because of the significance of quantum fluctuations in these compounds. In SrCuO<sub>2</sub>, an anomalous and anisotropic magnetic heat transport has been observed. By replacing the Sr with isovalent Ca it has been sought to separate this magnetic heat transport from the ordinary phononic heat transport. Surprisingly, the Ca suppresses also the magnetic heat transport. This has motivated further investigations of (Sr,Ca)CuO<sub>2</sub> with Nuclear Magnetic Resonance (NMR), a technique that directly probes the magnetic excitations through the coupling of the nuclear spins to the electronic spins. In the figure, the spin lattice relaxation rate,  $T_1^{-1}$ , of the copper nuclear spins is plotted versus temperature. For the pure compound,  $T_1^{-1}$  shows the typical, temperature independent behaviour that has been reported for other spin chain compounds, too [1]. Doping with 10 % Ca induces

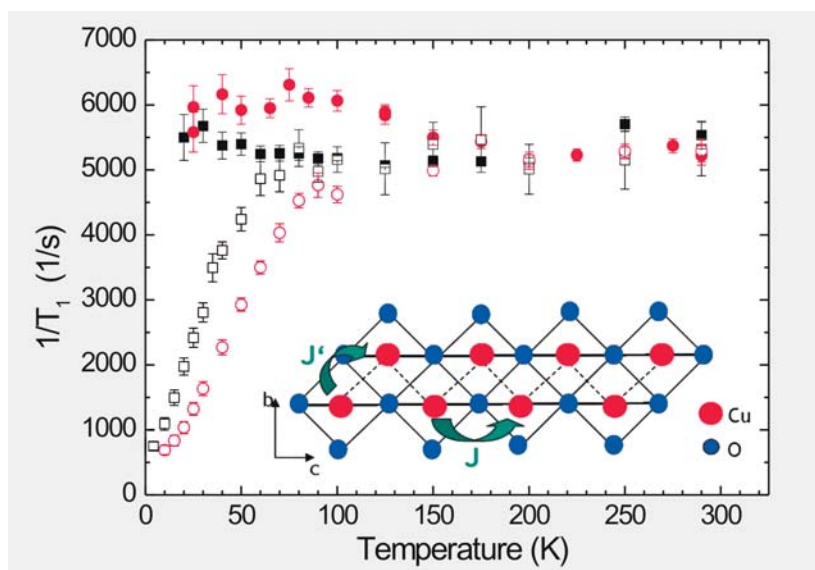


Fig.: <sup>63</sup>Cu NMR spin lattice relaxation rate,  $T_1^{-1}$ , versus temperature for the undoped SrCuO<sub>2</sub> (filled squares and circles), and the 10 % Ca doped SrCuO<sub>2</sub> (open squares and circles). Squares indicate external magnetic field,  $B$ , parallel the crystal axis  $c$ , circles indicate  $B \parallel b$ . Note the gap-like exponential decay for the Ca doped sample below  $T \sim 80$  K. Inset: copper oxide spin chains of SrCuO<sub>2</sub> with the antiferromagnetic intrachain coupling  $J$  and the ferromagnetic but frustrated interchain coupling  $J'$ .

a gap-like exponential decrease of  $T_1^{-1}$  for temperatures below 80 K. A possible explanation of this spin gap behaviour would be a Ca induced modification of the phonon states that induce local Spin-Peierls-Transitions in the spin chains, i.e. local, non-magnetic spin dimers.

[1] M. Takigawa *et al.*, Phys. Rev. Lett. (1996)

### Unusual interplay between structure, transport and magnetism in the new one-dimensional $S = 1/2$ system $\text{In}_2\text{VO}_5$

V. Kataev, M. Yehia, E. Vavilova, B. Büchner, A. Möller, T. Taetz, N. Hollmann, J. A. Mydosh

In the transition metal oxide  $\text{In}_2\text{VO}_5$ ,  $\text{V}^{4+}$  ( $3d^1$ ,  $S = 1/2$ ) ions are coupled via the oxygen ligands and realize a one-dimensional zig-zag spin-1/2 chain (Fig.). We have studied the structure, magnetization, electrical resistivity and nuclear- and electron spin resonance (NMR and ESR) of this compound [1]. The data reveal a remarkable interplay between lattice, spin and orbital degrees of freedom. At high temperatures  $\text{In}_2\text{VO}_5$  is semiconducting and exhibits ferromagnetic correlations in the spin sector. This is contrasted with the insulating behavior and predominantly antiferromagnetic (AFM) exchange between the localized  $\text{V}^{4+}$  spins below a characteristic temperature  $T^* \sim 120$  K. NMR measurements reveal a short-range quasi-static magnetic order at  $T_{\text{SRO}} \sim 20$  K but surprisingly no long-range ordered magnetic ground state can be observed. We attribute such an unusual crossover in the electronic and magnetic properties at  $T^*$  to the anisotropic thermal contraction of the lattice which yields magnetic frustration: Below  $T^*$  the  $c$ -axis continues to shrink whereas the  $b$ -axis begins to expand. The related changes in the overlap of the orbitals yield the localization of  $3d$ -electrons which AFM interact on a frustrated triangular pattern (Fig.). Transitions between different spin configurations give rise to an additional gapped ESR mode (Fig.) which is not expected in a spin-1/2 chain without frustration. The ESR gap  $f_0 \sim 100$  GHz gives the energy separation  $\Delta \sim 5$  K between the ground state  $S_{\text{tot}} = 1/2$  configuration of a frustrated spin triangle and its excited  $S_{\text{tot}} = 3/2$  state.

[1] A. Möller *et al.* Phys. Rev. B **76**, 134411 (2007)

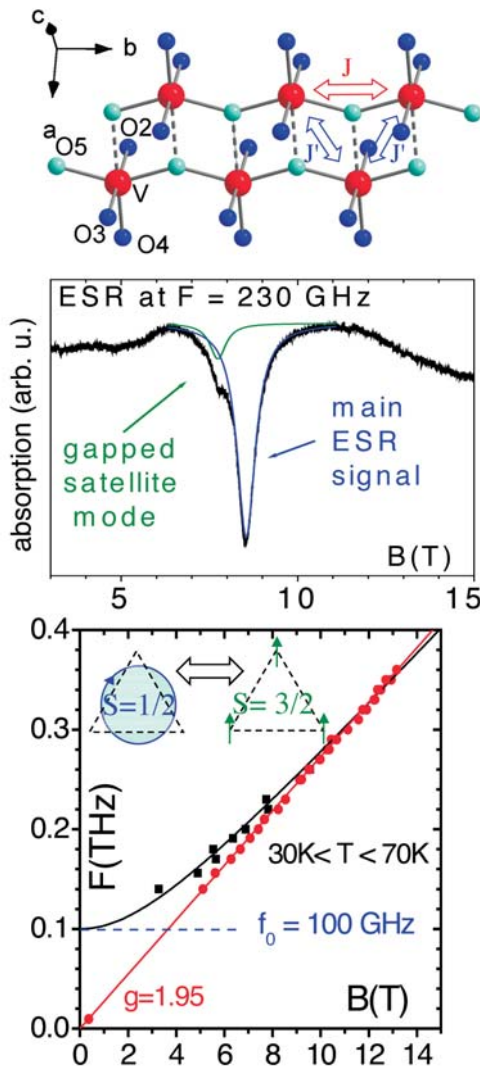
Fig.: (top) – V-O-V network in  $\text{In}_2\text{VO}_5$  forming a zig-zag spin-1/2 chain. The arrows indicate magnetic exchange paths  $J$  and  $J'$  of a comparable strength. Due to the AFM sign of  $J$  and  $J'$  below  $T^*$  the spin exchange is frustrated on a triangular pattern; (middle) – ESR spectrum at 230 GHz comprising the main signal and a weak satellite; (bottom) – ESR frequency versus resonance field dependence of the main and the satellite mode. The main branch (red) is gapless with a slope corresponding to the  $g$ -factor  $g = 1.95$  which is typical for  $\text{V}^{4+}$ . The satellite branch (black) has the same  $g$ -factor and exhibits a gap  $f_0 \sim 100$  GHz. This branch is due to the ESR transitions between different spin configurations occurring in the frustrated spin chain (see the text).

Cooperation Univ. of Cologne; Zavoisky Physical Technical Institute, Kazan, Russia

### Magnetic excitations of an undoped spin ladder

P. Ribeiro, N. Wizen, G. Behr, C. Hess, R. Klingeler, B. Büchner, S. Notbohm (1,2), B. Lake (1,3), D.A. Tennant (1,3), K.P. Schmidt (4), G.S. Uhrig (5), M. Reehuis (1,6), R. I. Bewley (7), C. D. Frost (7), P. Manuel (7), and R. S. Eccleston (8)

Low-dimensional quantum magnets have attracted much attention in recent years since unusual ground states and magnetic excitations are present, in particular, in quasi-one-dimensional spin systems. Moreover, such magnets serve as model systems for a comparison between experiment and theory, since exact solutions or numerical treatments of the model Hamiltonians yield clear-cut predictions. A frequently studied example is



the quantum-disordered spin-liquid state with a spin gap which is present in even-legged spin ladders. Experimentally, the compound  $(\text{Sr},\text{La},\text{Ca})_{14}\text{Cu}_{24}\text{O}_{41}$  is considered as one of the best representations of two-leg spin ladders with  $S=1/2$ . Despite being crucial for a thorough understanding of the physical properties of this intriguing material, an accurate determination of the magnetic excitation spectrum remained unresolved. A comprehensive investigation of the spin excitations has become feasible only recently through inelastic neutron scattering spectrometers with high reciprocal space resolution, combined with large energy transfer.

Using the 'Travelling Solvent Floating Zone'-method we have grown large single crystals of  $\text{La}_4\text{Sr}_{10}\text{Cu}_{24}\text{O}_{41}$  which contains undoped (hole-free) ladders and therefore can be considered as an ideal candidate for exploring the pure magnetic excitation spectrum. Inelastic neutron scattering has been performed using the MAPS spectrometer at ISIS, Rutherford Appleton Laboratory, U.K. In our measurements we could not only precisely reveal the one-triplon band, but could also investigate the two-triplon continuum (see figure). Our data directly reveal the spin gap  $\Delta = 26.4 \pm 0.3$  meV and through modeling the data based on the continuous unitary transformation method [1] the exchange constants  $J_{\text{leg}} = 186$  meV and  $J_{\text{rung}} = 124$  meV along the leg and rung, respectively, were obtained. Moreover, a substantial cyclic exchange of  $J_{\text{cyc}} = 31$  meV was found.

[1] S. Notbohm et al., Phys. Rev. Lett. **98**, 027403 (2007)

**Cooperations** Hahn-Meitner-Institut Berlin (1), Univ. of St. Andrews, United Kingdom (2), TU Berlin (3), École Polytechnique Fédérale de Lausanne, Switzerland (4), Univ. Dortmund (5), MPI Festkörperforschung, Stuttgart (6), ISIS Facility, Rutherford Appleton Laboratory, U. K. (7), Sheffield Hallam Univ., U.K. (8)

**Funded by** DFG

### First corrosion studies on Ni-Mn-Ga alloys for shape memory applications

A. Gebert, M. Dudek, S. Roth, U. Gaitzsch, L. Schultz

Investigations were started to characterize the corrosion behaviour of polycrystalline Ni-Mn-Ga alloys for shape memory applications. The  $\text{Ni}_{48}\text{Mn}_{30}\text{Ga}_{22}$  alloy stabilizes at room temperature a cubic austenite state, whereas the  $\text{Ni}_{50}\text{Mn}_{30}\text{Ga}_{20}$  alloy is in a tetragonal NM martensite state. Both alloys exhibit low corrosion rates and a spontaneous anodic passivation in alkaline solutions ( $\text{pH} = 8.4; 11$ ). In acidic media the alloys tend towards a more active state corresponding to a general shift of the corrosion potential to more negative values and an increase of the corrosion current density. While at  $\text{pH} = 5$  the alloys are still spontaneously passive upon anodization, in sulphuric acid solution with  $\text{pH} = 0.5$  a pronounced active-passive transition occurs before a passive state is attained by the formation of marginally protective surface layers (Figure).

Potentiostatic current transient measurements conducted at anodic passive potentials in electrolytes with  $\text{pH} = 5$  and  $8.4$  revealed a diffusion-controlled anodic passive layer growth. Under all conditions studied, but mostly pronounced in acidic environments, the martensite  $\text{Ni}_{50}\text{Mn}_{30}\text{Ga}_{20}$  alloy is significantly more reactive than the austenite  $\text{Ni}_{48}\text{Mn}_{30}\text{Ga}_{22}$  alloy. This can be attributed to a much higher density of surface defects in terms of a large number of twin boundaries, which can act as energetically favoured sites for corrosion attack. SEM analysis of the martensite  $\text{Ni}_{50}\text{Mn}_{30}\text{Ga}_{20}$  surface revealed a preferential corrosion following the pattern of the twin boundaries. But also the effect of a slightly lower content of Ga, which is the most stable alloy component at low pH values, must be considered.

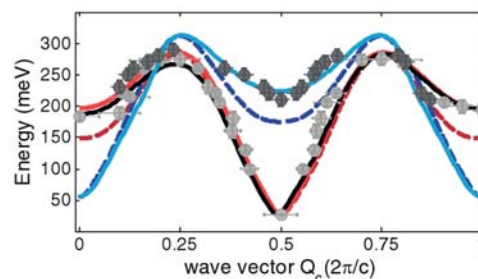


**Fig.:** Experimental results for the excitation spectrum of  $\text{La}_4\text{Sr}_{10}\text{Cu}_{24}\text{O}_{41}$  from neutron data. Light grey and dark grey data points denote the one-triplon and the lower bound of the two-triplon continuum, respectively. Theoretical one-triplon dispersion curves [1] are shown by solid red and black curves, where the black curve includes interladder coupling. The theoretical lower boundary of two-triplon scattering is shown by solid blue curve. Dashed lines show respective theoretical curves without taking cyclic exchange into account.

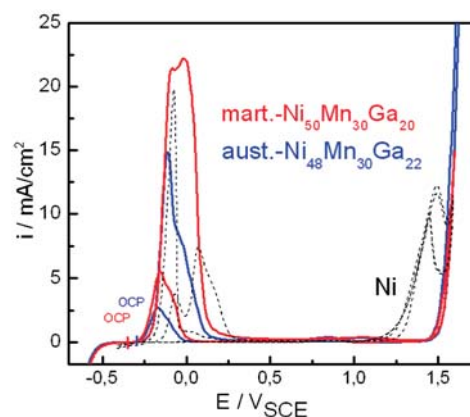


**Fig.:** Anodic polarization behaviour of Ni-Mn-Ga alloys in sulphuric acid solution with  $\text{pH} = 0.5$  in comparison to Ni.



Fig.: High resolution SEM micrograph of Ni-Mn-Ga fibres to be embedded into a polymer matrix.

## Magnetic Shape Memory Alloys

S. Fähler, S. Roth, O. Gutfleisch, M. Richter, U. Rößler, J. McCord, R. Schäfer, O. Heczko, L. Schultz, A. T. Onisan, N. S. Kiselev, A. Bogdanov, I. Opahle, Y. W. Lai, J. Liu, N. Scheerbaum, D. Hinz, U. Gaitzsch, M. Pötschke, J. Buschbeck, M. Thomas

Magnetic Shape Memory (MSM) alloys take a unique position within the class of smart materials due to their outstanding strain up to 10% obtained in a moderate magnetic field. The fundamental mechanism and observations of domain and variant movements are described in a separate highlight. The observed nucleation of new twin-variants and regular stripe-like microstructures have been calculated within a micromagnetic continuum approach. The results describe the magnetic field-induced transformation processes in single-crystalline slabs and free epitaxial films.

Whereas today mostly single crystals are used, textured NiMnGa samples prepared by directional solidification promise a more efficient way to produce active materials. Indeed after suitable thermal treatment for homogenization and ordering, followed by mechanical training, textured samples accomplished a magnetic field induced strain of about 1.5%. As an alternate approach for the efficient preparation of active bulk MSM material, single crystalline Ni<sub>2</sub>MnGa particles (see fig.) have been embedded in a polymer matrix. These composites show stress-induced twin boundary motion and are a promising candidate for the use as actuators or mechanical energy dampers.

For the integration into microactuator and sensors epitaxial Ni-Mn-Ga and Fe-Pd films have been grown. Though constrained by the substrate, orthorhombic Ni-Mn-Ga films exhibited a magnetically induced reorientation of martensitic variants. This could be explained by the additional freedom of an orthorhombic structure as compared to the usually examined tetragonal case. Epitaxial growth of disordered Fe-Pd has been achieved on substrates at room temperature. For this MSM system a significant expansion of the existence range of the martensite phase by stress was observed.

Density functional calculations show that the tetragonal distortion in Fe-Pd MSM alloys is due to a Jahn-Teller like effect in the Fe 3d minority spin states. Furthermore, disorder is found to be essential for the observed easy a-axis of magnetization in the fct phase.

Cooperation TU Dresden, Fraunhofer IWU Dresden, Plansee, Siemens AG, MPI MIS, Leipzig, Univ. Göttingen, Univ. Kiel, HMI Berlin, TU Braunschweig, Univ. Duisburg-Essen, Univ. Bonn, DLR Köln, TU Karlsruhe, Univ. des Saarlandes, HUT Helsinki, Donetsk PhysTech Institute, Lomonosov Moscow State Univ., Tomsk State Univ., MIT Boston, BSU Boise

Funded by DFG, SPP 1239 (coordinated at the IFW), BMBF

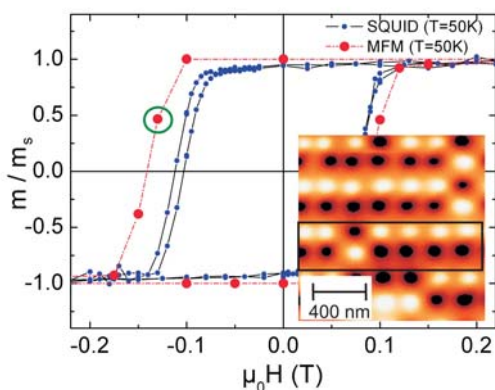


Fig.: Reconstruction of the magnetic hysteresis (red symbols) of exchange biased patterned Co/CoO dots by direct MFM imaging through a full field cycle. The magnetic state at -130 mT (green circle) is shown in the inset. The comparison with SQUID measurements (blue line) shows an overall good agreement but hints also towards inhomogeneities in the sample.

## Local magnetization studies by Magnetic Force and Kerr microscopy of exchange bias in arrays of Co/CoO dots

V. Neu, U. Wolff, S. Suck<sup>1</sup>, D. Givord<sup>1</sup>, S. Vock, T. Shapoval, C. Bran, M. Seifert, W. Rafelt, J. McCord, L. Schultz

Exchange-bias is known to originate from magnetic coupling at the interface between a ferro- and an antiferromagnet, but a clear description of this phenomenon is still missing. The complicating influence of structural and magnetic defects is expected to be considerably reduced at the nanoscale, when the single crystalline and single domain state is entered. Thus, in the present study the magnetization behaviour of arrays of small Co/CoO dots ( $120 \times 360 \text{ nm}^2$ ) has been investigated by magnetic force (MFM) and Kerr microscopy at low temperatures ( $T = 50 \text{ K}$ ).

Patterned Co/CoO samples were prepared by electron beam lithography with a subsequent

lift-off technique. For MFM imaging, the sample was cooled through the Néel temperature in a positive in-plane field within the microscope. In zero field, the fully in-plane magnetized rectangles show up as rows of black and white spots arising from the magnetic charges building up at the element edges. When negative fields are applied, the elements individually switch their magnetization direction, which is observed as a sudden reversal of the MFM contrast. An example is shown at a field of -130 mT. Evaluating the total magnetization of the imaged area throughout a full field cycle we can construct the hysteresis curve (red symbols). The comparison with the global magnetization measurements (blue line,  $H_c = 94$  mT,  $H_b = 17$  mT) shows an overall good agreement but the larger coercivity obtained on a well structured sample area also hints towards inhomogeneities on a larger scale.

Other current activities of the magnetic force microscopy group include domain studies of extended [Co/Pt]/Ru multilayers, CoPt multilayers on self assembled nanospheres and development of MFM tip coatings for improved imaging quality.

**Cooperations** Univ. Göttingen, Univ. Chemnitz, <sup>1</sup>LLN Grenoble, Hitachi GST San José  
**Funded by** EU (Hiperchem), DFG (SFB 463)

### Epitaxial PrCo<sub>7</sub> films with high energy density

A. K. Patra, V. Neu, S. Fähler, L. Schultz

Research on RE-Co magnets with a TbCu<sub>7</sub> structure has been intensified in recent years because of their potential as permanent magnets for high temperature applications. RECo<sub>7</sub> magnets display a unique combination of intrinsic properties such as a high saturation polarization, a high Curie temperature and a room temperature uniaxial anisotropy. However, the hexagonal RECo<sub>7</sub> is a metastable structure and often cannot be prepared without a stability element, or it transforms into the stable rhombohedral RE<sub>2</sub>Co<sub>17</sub> structure upon applying higher temperature.

By using nonequilibrium growth technique like pulsed laser deposition, we could prepared epitaxial binary Pr-Co films with a disordered PrCo<sub>7</sub> structure (TbCu<sub>7</sub> type), without the addition of any stabilizing elements [1]. These Pr-Co films prepared on a Cr buffered MgO(110) at a substrate temperature of 450°C to 600°C, grow epitaxially with a (100) texture having the c-axis of the hexagonal Pr-Co grains uniquely aligned along the MgO[001] (see Fig). Moreover, Pr-Co films prepared at 450°C maintain their PrCo<sub>7</sub> structure even after being exposed to high post annealing temperatures of 800°C [2]. In the optimum conditions, these PrCo<sub>7</sub> films exhibit an energy product value of  $(BH)_{\max} = 345$  kJ/m<sup>3</sup>, which is the highest value ever reported for a RE-Co magnet [2].

[1] A. K. Patra *et al.*, *Phy. Rev. B*, **75**, 184417 (2007).

[2] A. K. Patra *et al.*, *J. Phys. D: Appl. Phys.* **40**, 7261 (2007).

**Cooperation** FZ Dresden-Rossendorf, TU Dresden, Univ. Duisburg-Essen

**Funded by** SFB 463 (B20)

### Measuring strain-dependent properties of magnetic oxide films

O. Bilani-Zeneli, M. C. Dekker, K. Dörr, R. B. Gangineni, A. Herklotz, J.-W. Kim, K. Nenkov, D. Rata, L. Schultz

Mechanical strain as a consequence of lattice mismatch is common to nearly all epitaxially grown films and multilayers. Another consequence may be the formation of lattice defects such as dislocations or vacancies. For highly correlated oxides, strikingly large strain-induced changes of their electronic properties (ferroelectric polarization,

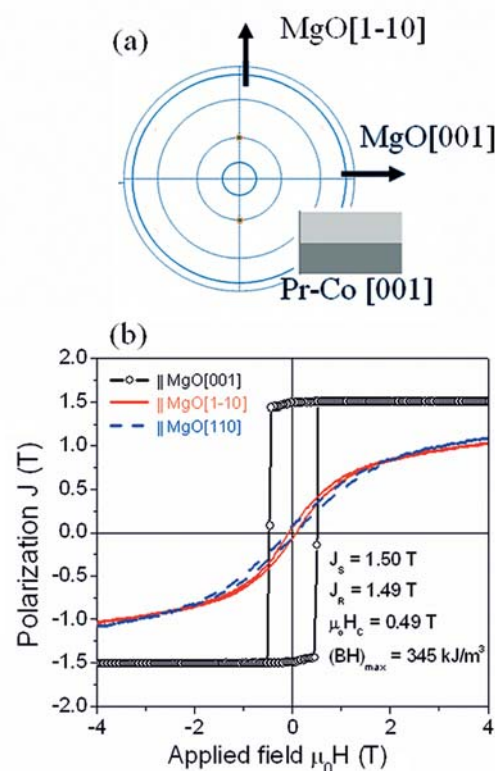
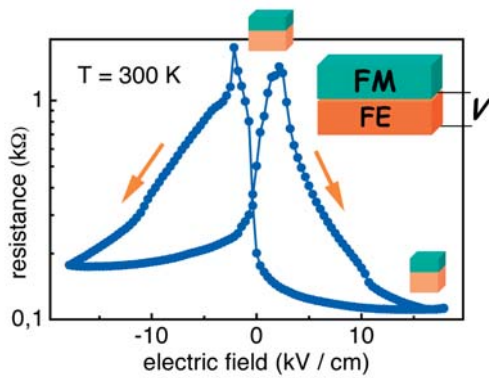


Fig.: (a) Pr-Co(110) pole figure and (b) room temperature hysteresis loops measured with field parallel to MgO[001], [1-10] and [110] directions for a PrCo<sub>7</sub> film.



**Fig.:** Strain-dependent resistance of an epitaxially grown  $\text{La}_{0.7}\text{Sr}_{0.3}\text{CoO}_3/\text{PMN-PT}(001)$  film vs. the electric field applied to the substrate. The substrate in-plane lattice parameter biaxially shrinks by about 0.011% per 1 kV/cm.

electrical conductivity, magnetization, superconductivity) have been predicted and reported in recent years.

We proposed an experimental method for the *unambiguous measurement* of biaxial epitaxial *strain effects* in thin films, which relies on growing the investigated material on a monocrystalline piezoelectric substrate.  $\text{Pb}(\text{Mg}_{1/3}\text{Nb}_{2/3})_{0.72}\text{Ti}_{0.28}\text{O}_3$  (PMN-PT(001)) with a pseudocubic lattice structure close to that of  $\text{LaAlO}_3$ , except for the larger lattice parameter of 4.022 Å, allows one to electrically control the substrate in-plane lattice parameter. The piezo-strain is nearly linear, reversible and sufficiently uniform in a range of up to 0.4%. Model systems for the *elastic magnetoelectric coupling* have been investigated for magnetic oxides  $\text{La}_{1-x}\text{A}_x\text{MO}_3$  ( $M = \text{Mn}$  or  $\text{Co}$ ,  $A = \text{Sr}$ ,  $\text{Ca}$ ,  $\text{Ce}$ ) epitaxially grown on PMN-PT. Efficient electrical control of the magnetization (which lies in the film plane) is observed for  $\text{La}_{0.7}\text{Sr}_{0.3}\text{MnO}_3/\text{PMN-PT}(001)$  at ambient temperature. While manganite films of various compositions show an enhanced strain sensitivity of the conductivity, an extreme impact of tensile strain on the conductivity of  $\text{La}_{0.7}\text{Sr}_{0.3}\text{CoO}_3$  films is detected (see Fig.), which are insulating with resistive gauge factors above 1000 at 300 K. First strain experiments on lateral structures are conducted for step edge tunnel junctions in films grown over etched steps in PMN-PT(001).

**Cooperation** Oak Ridge National Laboratory, TU Dresden, Univ. Bonn, Univ. Hamburg  
**Funded by** DFG, FOR520, IMPRS, DAAD, Leibniz Pact 2006

### Magnetic field dependent structure of $\text{TbFe}_3(\text{BO}_3)_4$

M. Philipp, O. Kataeva, J. E. Hamann-Borrero, C. Hess, R. Klingeler, N. Tristan, B. Büchner, M. von Zimmermann (1), A. Vasiliev (2), L. N. Bezmaternykh (3)

The rare-earth ferro-borate family  $\text{RFe}_3(\text{BO}_3)_4$  ( $R$  rare earth or Y) exhibits a multitude of phases, including multiferroicity for  $R = \text{Gd}$  and  $\text{Nd}$ . In all these compounds the iron ions order antiferromagnetically below  $T_N \approx 40$  K. In the case of  $\text{TbFe}_3(\text{BO}_3)_4$  the iron subsystem has an antiferromagnetic easy axis parallel to the  $c$ -axis, which polarizes the terbium moments as well. At low temperature the iron spins flop into the  $ab$ -plane upon the application of a magnetic field parallel to the  $c$ -axis ( $B_c(2\text{K}) \approx 3.5\text{T}$ ). Concomitantly, the Tb-moments align ferromagnetically so that a sharp metamagnetic transition is observed at  $B_c$  [1] (cf. Fig. b). In order to analyze structural distortions accompanying these transitions, X-ray diffraction experiments on  $\text{TbFe}_3(\text{BO}_3)_4$  were performed using synchrotron radiation with a photon energy of 100 keV. The sample was located inside a cryostat with a magnet insert, which could generate magnetic fields up to 8 T.

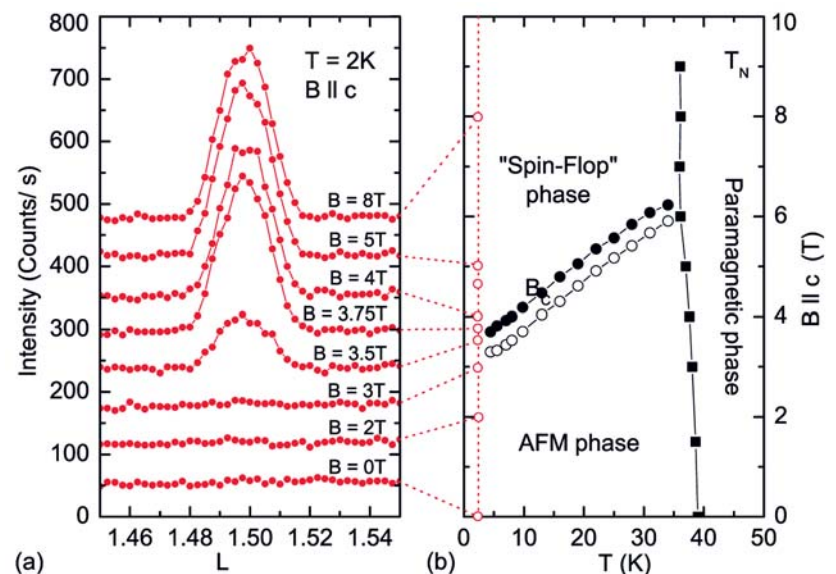


**Fig.:** (a) Magnetic field dependence of the superstructure reflection (0,0,1.5).  
 (b) Magnetic phase diagram of  $\text{TbFe}_3(\text{BO}_3)_4$ .

Our data clearly reveal a weak superlattice reflection at  $(0,0,1.5)$  upon the application of a magnetic field  $B > B_c$  parallel to the  $c$ -axis (see Figure a). According to the reflection conditions of the space group  $P3_121$ , this reflection is a satellite of the first allowed main reflection at  $(0,0,3)$ . This implies a doubling of the unit cell in  $c$ -direction, which apparently is only present in the spin-flop phase. Measurements on other compounds of the family ( $R = \text{Gd, Nd, Y}$ ) indeed clearly show a correlation between the “easy-plane” alignment of the iron spins, which in the case of  $R = \text{Tb}$  is realized in the spin-flop phase, and the twofold structural modulation. Our results give a strong evidence for a significant magneto-elastic coupling in  $\text{TbFe}_3(\text{BO}_3)_4$ , which is an important prerequisite for multi-ferroicity with magneto-electric coupling.

[1] E.A. Popova et al., Phys. Rev. B **75** 224413 (2007).

**Cooperations** HASYLAB@DESY (1), Moscow State Univ., Russia (2), L.V. Kirensky Institute of Physics, Krasnoyarsk, Russia (3)

**Funded by** DFG, Leibniz Pact 2006

### High pulsed magnetic fields

J. Freudenberger, N. Kozlova, K.-H. Müller, K. Dörr, W. Häbeler, M. Herrmann, L. Schultz, R. Klingeler, N. Tristan, A. Bajpai, N. Leps, C. Golze, V. Kataev, B. Büchner

The dynamics of electrons in a semiconductor superlattice was investigated under the action of large applied electric and magnetic fields. In this study the volt-ampere characteristic of the superlattices was measured at the top of the magnetic field pulse. It was observed that the coupling of the Bloch and cyclotron oscillations in the tilted magnetic field geometry generates a magnetic field-induced miniband structure and an extended electron motion across many periods of the superlattice. The spatially extended character of the electronic states is analogous to the delocalization of the electron orbit in a semiclassical description of the electron motion and explains the observation of a strong resonant enhancement of the current flow through the superlattice.

The topics of high-field research also included measurements of irreversibility and upper critical fields of superconductor  $\text{MgB}_2$  doped with carbon, field-induced transition in non-centrosymmetric heavy-fermion superconductor  $\text{CePt}_3\text{Si}$ , magnetotransport of cobaltite thin films, magnetostriction field-induced transition in  $\text{GdSi}$  single crystal. A series of experiments on the dilute nitride alloy  $\text{GaAs}_{1-x}\text{N}_x$  ( $x = 0.1\%$ ) showed a strong magnetophonon resonance effect. In addition, we have measured high field magnetization, specific heat, resistivity and ESR in order study molecular magnets, highly frustrated quasi-1D spin chains in  $\text{Li}_2\text{ZrCuO}_4$ , the interplay of Haldane physics and classical spins in  $\text{Y}_{2-x}\text{Nd}_x\text{BaNiO}_5$ , the effect of grain boundaries on the magneto-resistance in  $\text{CrO}_2$  and the multiferroic properties of rare-earth ferrobates  $\text{RFe}_3(\text{BO}_3)_4$ .

**Cooperation** FZ Dresden Rossendorf, TU Dresden, Univ. of Nottingham, Univ. of Oxford, Charles Univ. Prague, LNCMP Toulouse, Warsaw Univ., HMFL Nijmegen.

**Funded by** EuroMagNET, EU contract 506239, EU Marie Curie IIF NewMatCr

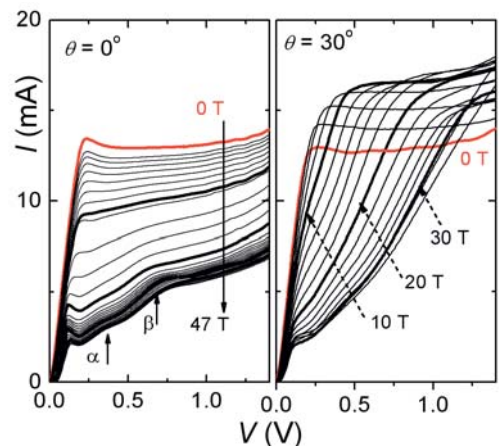


**Fig.:** Dependence of the current-voltage,  $I(V)$ , curve at  $T = 4.2 \text{ K}$  on magnetic field,  $B$ , applied (a) along and (b) tilted at angle  $\theta = 30^\circ$  to the superlattice axis.  $B$  is increased from 0 to 47 T. The weak dependence on  $B$  of resonances  $\alpha$  and  $\beta$  at high  $B$  ( $> 25 \text{ T}$ ) indicates a strong polaron pinning effect associated with the electron-phonon interaction.

## Thermodynamic properties of rare-earth ferrobates

N. Leps, M. Philipp, L. Wang, J. Leschner, N. Tristan, R. Klingeler, B. Büchner, C. Hess, E.A. Popova (1), A.N. Vasiliev (1)

Rare-earth ferrobates with the general composition  $R\text{Fe}_3(\text{BO}_3)_4$  ( $R$  = rare-earth ion or Y) exhibit a variety of interacting ordering phenomena. Interestingly, at least the compounds with  $R = \text{Nd}, \text{Gd}$  show multiferroic properties. The strong interaction of magnetic, structural and dielectric degrees of freedom basically results from a long range antiferromagnetic ordering of the Fe sublattice which spins are coupled to the rare earth moments. One example is  $\text{TbFe}_3(\text{BO}_3)_4$ , the magnetisation of which exhibits a sharp metamagnetic transition in the AFM Fe-spin ordered phase upon application of a magnetic field along the easy magnetic  $c$ -axis [1]. At the transition, the Fe-spins undergo a spin-flop transition which is associated to the ferromagnetic alignment of the anisotropic  $\text{Tb}^{3+}$ -ions. The metamagnetic transition is accompanied with pronounced magnetostrictive effects, e.g. a shrinking of the  $c$ -axis by  $\Delta c/c \sim 2 \cdot 10^{-5}$ , which presumably arises due to the large spin-orbit coupling of the 4f electrons of the  $\text{Tb}^{3+}$ -ions. Substituting the rare earth ion ( $R = \text{Nd}$  [3,5], Dy [6] or Cr for Fe [4] modifies this interplay but corroborates the interpretation.

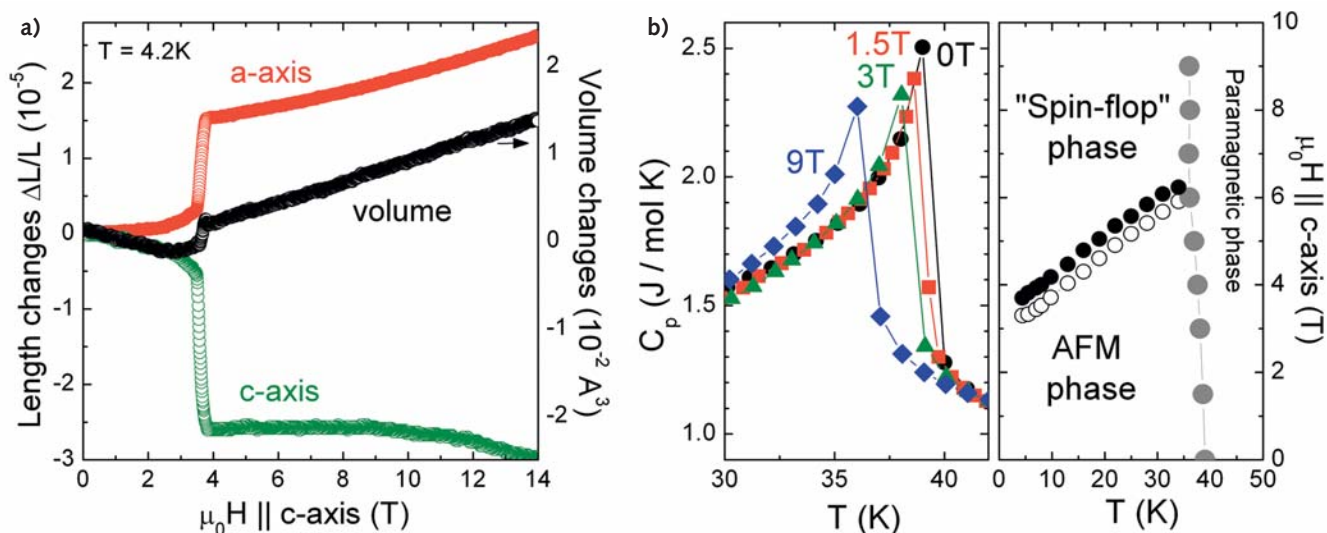


Fig.: a) Magnetostriction of  $\text{TbFe}_3(\text{BO}_3)_4$  at  $T = 4.2 \text{ K}$  versus magnetic field applied parallel to the  $c$ -axis. b) Specific heat vs. temperature around  $T_N$  in different magnetic fields (left) and magnetic phase diagram (right).

- [1] E.A. Popova et al., Phys. Rev. B 75 (2007) 224413
- [2] N. Tristan et al., JMMM 316 (2007) e621
- [3] D.V. Volkov et al., JMMM 316 (2007) e717
- [4] E.A. Popova et al., Phys. Rev. B 76 (2007) 54446
- [5] E.A. Popova et al., JETP 105 (2007) 105-107
- [6] E.A. Popova et al., Phys. Rev. B, submitted

**Cooperations** Moscow State University (1), Moscow, Russia, L.V. Kirensky Institute of Physics, Krasnoyarsk, Russia, Bryansk State Technical University, 241035 Bryansk, Russia, HASYLAB @ DESY, Hamburg

**Funded by** DFG (FOR 520), DFG German-Russian Joint Laboratory

## Research Area 3

### Molecular nanostructures and molecular solids

#### The electronic properties of potassium doped copper-phthalocyanine

K. Flatz, M. Grobosch, M. Knupfer

Doped molecular crystals are predicted to show a variety of fundamentally new physical properties. Recent theoretical work, for instance, has led to intriguing predictions such as the formation of novel strongly correlated metals in the family of electron doped phthalocyanines or of quasi-one dimensional potassium-oxygen chains in doped PTCDA thin films. We have studied the evolution of the electronic structure of copper phthalocyanine (CuPc) thin films upon K doping using electron energy-loss spectroscopy (EELS) in transmission. Our results demonstrate the formation of distinct, stable  $K_x\text{CuPc}$  phases. In particular, the consideration of the C1s and K2p core level excitations and recent results by Giovannelli *et al.* (J. Chem. Phys. **126**, 044709 (2007)) allows to conclude that these phases have the stoichiometry  $K_2\text{CuPc}$  and  $K_4\text{CuPc}$ . In addition, we have analyzed the evolution of the electronic excitations of these phases, which is shown in the Figure. Our results indicate that both doped phases are insulators with a quite complex excitation spectrum. For details see K. Flatz *et al.*, J. Chem. Phys. **126**, 214702 (2007).

Cooperation Univ. Zürich

Funded by Socrates Erasmus Program

#### In situ ESR-UV/VIS/NIR spectroelectrochemistry of an empty fullerene anion and cation: the $C_{82}:3$ isomer

M. Zalibera, P. Rapta, L. Dunsch

The application of in situ ESR-UV/VIS/NIR spectroelectrochemistry to the highly purified  $C_{82}:3$  fullerene isomer with  $C_2$  symmetry made the detailed characterization of the radical structures formed by electrochemical generation possible. This first comprehensive spectroelectrochemical study on the stable radical anion and cation of an empty cage higher fullerene in acid-free organic electrolyte is a contribution to the general understanding of charged states at endohedral fullerenes. We have generated electrochemically the stable radical anion and cation of an empty fullerene in acid free solution at room temperature as confirmed by *in situ* ESR-UV/VIS/NIR spectroelectrochemistry. Additionally, well defined characteristic VIS/NIR bands for the solvated monoanion as well as the solvated monocation of the  $C_{82}:3$  fullerene isomer were measured enabling a detailed description of the electronic structure of monocharged  $C_{82}$  fullerene. Comprehensive studies on  $C_{82}:3$  isomer including isolation, structure, spectroscopy, spectroelectrochemistry and theoretical DFT calculations are currently underway in our group.

Cooperation Slovak Technical Univ. Bratislava, Slovakia

Funded by Humboldt foundation

#### Carbon nanoparticles for hydrogen storage

H. Hermann, M. Hentsche, O. Khvostikova, D. Lindackers, Th. Gemming, H. Wendrock

Detailed microstructural analyses of ball-milled nanostructured graphitic carbon and the comparison of the microstructural parameters with the results of low-temperature hydrogen storage experiments showed that the results for the storage capacity can be understood assuming the following sequence of processes: At 110 K and pressure of the

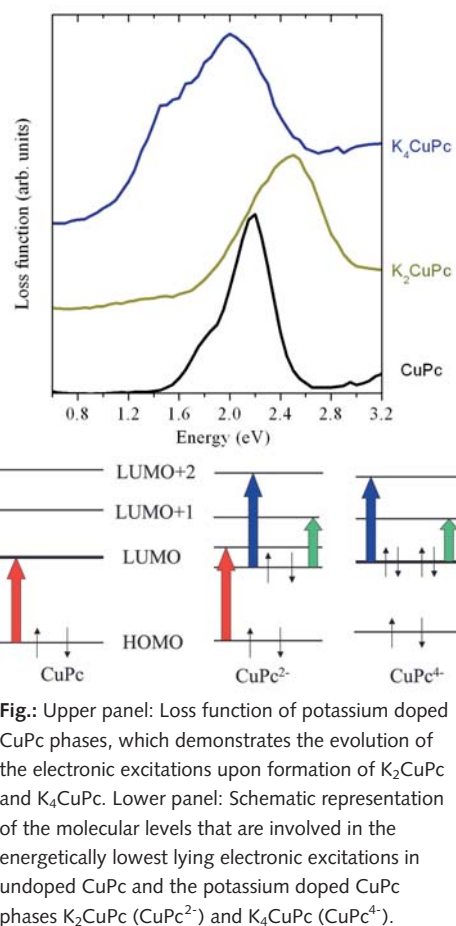


Fig.: Upper panel: Loss function of potassium doped CuPc phases, which demonstrates the evolution of the electronic excitations upon formation of  $K_2\text{CuPc}$  and  $K_4\text{CuPc}$ . Lower panel: Schematic representation of the molecular levels that are involved in the energetically lowest lying electronic excitations in undoped CuPc and the potassium doped CuPc phases  $K_2\text{CuPc}$  ( $\text{CuPc}^{2-}$ ) and  $K_4\text{CuPc}$  ( $\text{CuPc}^{4-}$ ).

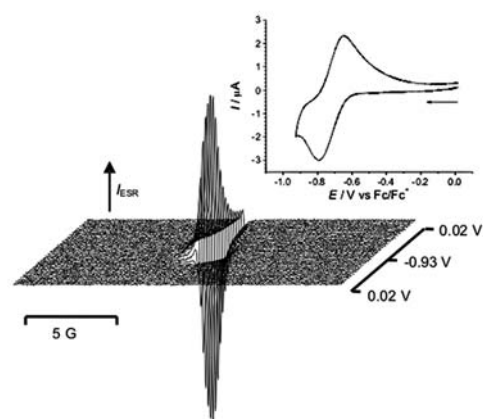


Fig.: Potential dependence of the ESR spectrum of the  $C_{82}:3^{3-}$  anion radical observed by *in situ* spectroelectrochemistry. Inset: Cyclic voltammogram of  $C_{82}:3$  isomer in TBAPF<sub>6</sub>/o-DCB solution for the first reduction step (Pt-mesh working electrode, scan rate 3.00  $\text{mV s}^{-1}$ ) in the spectroelectrochemical cell.

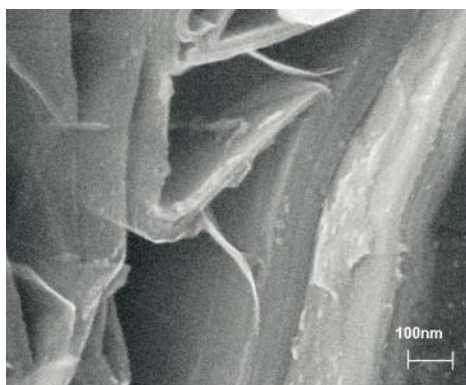


Fig.: SEM image of porous carbon.

order of 10 MPa the trapping states at the surface are getting filled. Increasing the pressure to 20 MPa at 110 K small micropores are partially filled. At 77 K and pressure of 10 MPa all small micropores are filled. In the temperature range of 35 K to 40 K and pressure above 2 MPa multilayer adsorption takes place in the mesopores. The conditions of 35 K to 40 K and 2 MPa are not so far from the critical point of hydrogen. One may argue the presence of graphene surfaces could shift the critical point to higher temperatures. In this case one could speak about capillary condensation. However, we did not find hysteresis effects during the temperature-pressure cycles. Assuming the presence of capillary condensation the absence of hysteresis effects suggests that only pores with diameters less than 4 nm contribute to the observed effects [1]. Current research is concentrated on the preparation of nanostructured carbon with high specific surface area and high fraction of nanopores. Fig.1 shows a SEM image of porous graphite. Porous graphite of this topology but with smaller dimension is considered to be promising for improving the hydrogen storage capacity.

[1] M. Hentsche et al. Int. J. Hydrogen Energy 32 (2007) 1530-1536.

Cooperation TU Dresden

Funded by Stiftung Energie Baden-Württemberg

### Electronic Structure and Electrochemical Properties of the $C_{60}(CF_3)_n$ Fullerenes

A. A. Popov, I. E. Kareev, N. B. Shustova, E. B. Stukalin, S. F. Lebedkin, K. Seppelt, S. H. Strauss, O. V. Boltalina, L. Dunsch

The frontier orbitals of 22 isolated and characterized  $C_{60}(CF_3)_n$  derivatives, have been investigated by electronic spectroscopy ( $n = 2, 4, 6, 8, 10, 12$ ; the number of isomers for each composition is shown in square brackets), fluorescence spectroscopy ( $n = 10$ ), cyclic voltammetry under air-free conditions (all compounds with  $n \leq 12$ ), ESR spectroscopy of  $C_{60}(CF_3)_n^-$  radical anions at 25 °C ( $n = 4$  and 10), and quantum chemical calculations at the DFT level of theory (all compounds including  $n = 16$  and 18). DFT calculations are also available for several hypothetical  $C_{60}(CF_3)_n$  derivatives. The X-ray structure of one of the compounds, 1,6,11,16,18,26,36,41,44,57- $C_{60}(CF_3)_{10}$ , is given for the first time. Most of the compounds with  $n \leq 12$  exhibit two or three quasi-reversible reductions at scan rates from 20  $mV s^{-1}$  up to 5.0  $V s^{-1}$ , respectively. The 18 experimental  $0/-E_{1/2}$  values (vs.  $C_{60}^{0/-}$ ) are a linear function of the DFT-predicted LUMO energies (average  $E_{1/2}$  deviation from the least-squares line is 0.02 V). This linear relationship was used to predict the  $0/-E_{1/2}$  values for the  $n = 16$  and 18 derivatives, and none of the predicted values is more positive than the  $0/-E_{1/2}$  value for one of the isomers of  $C_{60}(CF_3)_{10}$ . In general, reduction potentials for the  $0/-$  couple are shifted anodically relative to the  $C_{60}^{0/-}$  couple. However, the  $0/-E_{1/2}$  values for a given composition are strongly dependent on the addition pattern of the  $CF_3$  groups. In addition, LUMO energies for isomers of  $C_{60}(X)_n$  ( $n = 2, 4, 6, 8, 10, 12$ ) that are structurally related to many of the  $CF_3$  derivatives were calculated and compared for  $X = CH_3, H, Ph, NH_2, CH_2F, CHF_2, F, NO_2,$  and  $CN$ . The experimental and computational results for the  $C_{60}(CF_3)_n$  compounds and the computational results for more than 50 additional  $C_{60}(X)_n$  compounds provide new insights about the frontier orbitals of  $C_{60}(X)_n$  derivatives. For a given substituent, X, the addition pattern is as important, if not more important in many cases, than the number of substituents,  $n$ , in determining  $E_{1/2}$  values. Those addition patterns with double bonds in pentagons having two  $C(sp^2)$  nearest neighbors result in the strongest electron acceptors.

Cooperation Moscow State Univ., Russia; Univ. of Colorado, Ft. Collins, USA

Funded by DAAD

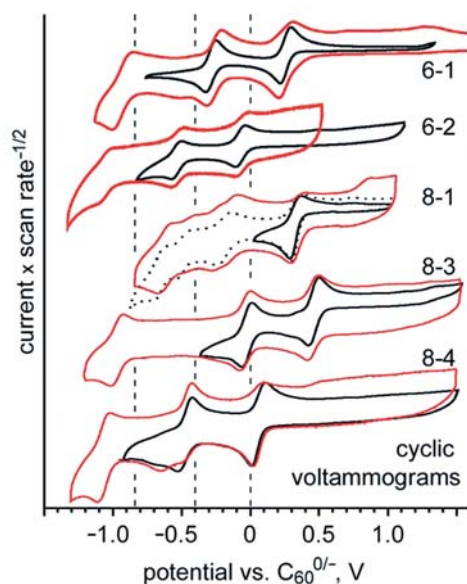
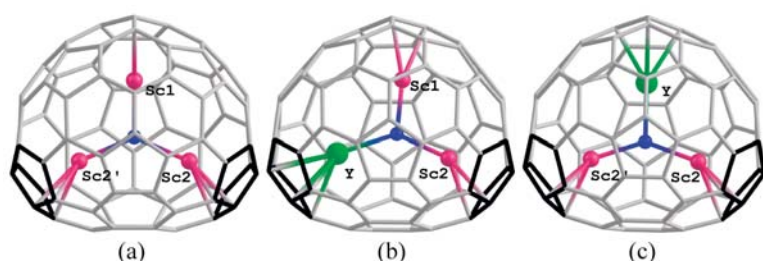


Fig: Cyclic voltammograms of the two isomers of  $C_{60}(CF_3)_6$  and three of the five isomers of  $C_{60}(CF_3)_8$  (0.10 M  $TBA^+BF_4^-$  in  $CH_2Cl_2$ ; the scan rate for the black voltammograms was 20  $mV s^{-1}$ ;  $E_{1/2}(C_{60}^{0/-}) = -0.98$  or  $-0.46$  V vs.  $Fe(Cp)_2^{+/0}$  or  $Fe(Cp^*)_2^{+/0}$  internal standards, respectively). The vertical dotted lines show the first, second, and third reduction  $E_{1/2}$  values for  $C_{60}$  under identical conditions.

## An Endohedral $C_{76}$ Fullerene Cage: the first Non-IPR $DySc_2N@C_{76}$

S. Yang, A. A. Popov, L. Dunsch

We have successfully synthesized and isolated  $DySc_2N@C_{76}$  — the first non-IPR  $C_{76}$ -cage filling the gap of the cages available in nitride clusterfullerenes.  $DySc_2N@C_{76}$  is a stable fullerene with a small band-gap of 0.96 eV. FTIR spectroscopic study in combination with extensive DFT calculations accomplishes the assignment of the non-IPR  $C_{5:17490}$ -I isomer as the cage structure of  $DySc_2N@C_{76}$ , as convinced by the good coincidence of the computed IR spectrum of  $YSc_2N@C_{76}$  and the experimental spectrum of  $DySc_2N@C_{76}$  as well as of their optical band-gap.  $DySc_2N@C_{76}$  provides the first example of stabilization of the non-IPR  $C_{76}$  cage by encapsulation of an asymmetric  $DySc_2N$  mixed cluster, revealing the role of the cluster structure on the stability of the fullerene cage. As the asymmetric  $DySc_2N$  cluster has a more suitable geometry for the inner space of the  $C_{76}$  cage compared to the homogeneous clusters like  $Sc_3N$  or  $Dy_3N$ , the highest yield for  $C_{76}$ -based clusterfullerenes with the  $Dy_xSc_{3-x}N$  mixed nitride cluster is achieved for the  $DySc_2N@C_{76}$ . This result points to the role of the cluster geometry and opens a new avenue for synthesizing novel non-IPR endohedral fullerenes.



**Fig.:** DFT-optimized structure of  $Sc_3N@C_{76}$  (a),  $YSc_2N@C_{76}$ -I (b), and  $YSc_2N@C_{76}$ -II (c). The  $C_{76}$  cages are all based on  $C_{5:17490}$  symmetry. Two pairs of the adjacent pentagons are highlighted in black. The assigned cage structure of  $DySc_2N@C_{76}$  is same to that of  $YSc_2N@C_{76}$ -I (b).

Cooperation Moscow State Univ., Russia  
Funding by DAAD

## An in situ ESR UV-vis-NIR spectroelectrochemical study of the anodic aromatic diamine oxidation

A. Goux, D. Pratt, L. Dunsch

The combination of two spectroscopic methods, ESR spectroscopy and UV-visible-NIR spectroscopy, with voltammetric techniques applied in situ has allowed the clarification of the reaction mechanism of the anodic oxidation of *p*-toluenediamine at different pH 2, 4, 7 and 10 and the limited range for the existence of a stable radical intermediate. At all pH values, a quinoid *p*-toluenediimine intermediate and a trimeric reaction oxidation product, a Bandrowski's base derivative, have been detected by in situ UV-vis spectroscopy. At pH 4-7, a further intermediate, the semiquinone radical, has been detected both by in situ ESR and simultaneously applied in situ UV-vis spectroscopy. A mechanism of the oxidation of *p*-toluenediamine is proposed which takes into account the role of the radical species in the oxidation steps and their pH dependence in aqueous solutions. At very acidic and alkaline pH values, a two-electron oxidation leads to the formation of the quinoid diimine structure. At intermediate pH values, a first one-electron oxidation leads to the formation of the semiquinone radical, which is then oxidized in a second one-electron step into the quinoid diimine. The latter reacts with a further *p*-toluenediamine molecule to give a dimer. Finally, this dimeric compound reacts with another diimine structure which is reduced in a two single-electron step to give a trimeric product with a structure similar to Bandrowski's base.

Cooperation KPSS Darmstadt  
Funded by KPSS Darmstadt

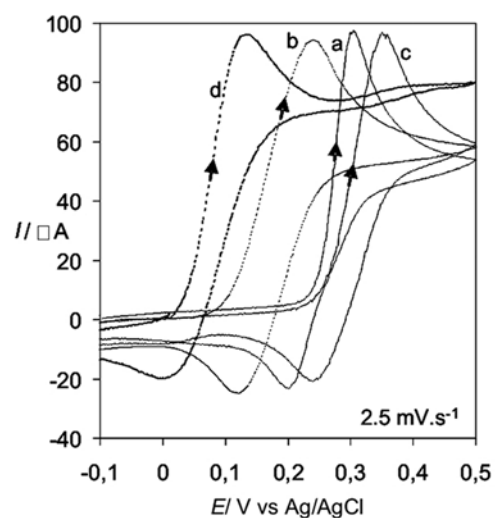


**Fig.:** Cyclic voltammograms of an aqueous  $5 \text{ mmol L}^{-1}$  *p*-toluenediamine solution at pH 2 (a), 4 (b), 7 (c) and 10 (d); sweep rate  $2.5 \text{ mV.s}^{-1}$ , Pt working electrode.

## Charge injection and transport in poly[N-methyl(aniline)]

A. Petr, Di Wei, C. Kvarnström, L. Dunsch, A. Ivaska

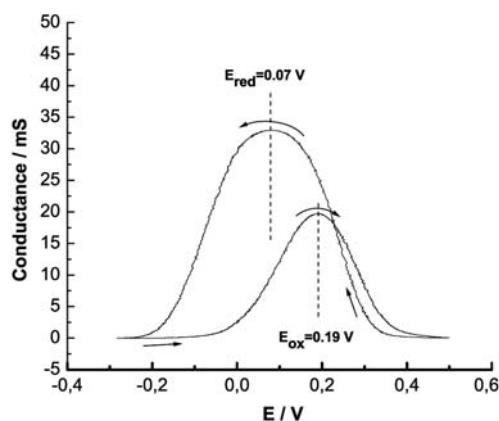


Fig.: In situ conductance measurement during electrochemical doping of a PNMA film.

In situ electron spin resonance (ESR) and UV-vis-NIR measurements have been carried out during oxidation of a poly[N-methyl(aniline)] (PNMA) film, which was prepared electrochemically in aqueous solutions containing 1 M trifluoroacetic acid. Simultaneous conductance measurements were also performed during the electrochemical doping of PNMA. The combination of the different experimental techniques allows a simultaneous elucidation of optical and electrochemical properties of the conducting polymer film. Although there are a lot of predictions and discussions on the free charge carriers of poly(aniline) (PANI) and its derivatives, there is no direct evidence of the correlation between polarons and conductance for PANI and its derivatives during doping. Our work provides the correlation between the spin and spinless species and the conductance of PNMA during the electrochemical doping in acidic aqueous solutions as shown in the Fig. PNMA differs from other conjugated polymers (eg. polypyrrole, polythiophene) in that the results from ESR and *in situ* conductance are consistent. At higher doping (oxidation) levels, the conductance decreases with the decrease in the ESR signal indicating that there is no spinless bipolaronic conducting state in PNMA. Polaron pairs are supposed to be responsible for these decreases.

Cooperation Process Chemistry Centre, Abo Akademi University, 20500 Abo/Turku, Finland

Funded by DAAD

## The in situ Raman spectroelectrochemical study of $^{13}\text{C}$ labeled fullerene peapods and double walled carbon nanotubes

M. Kalbáč, L. Kavan, M. Zukalová, L. Dunsch

The  $\text{C}_{60}$  fullerene peapods and double walled carbon nanotubes (DWCNTs) containing highly  $^{13}\text{C}$  enriched  $\text{C}_{60}$  and inner tubes, respectively have been studied using Raman spectroscopy and in-situ Raman spectroelectrochemistry in order to follow the influence of  $^{13}\text{C}$  enrichment on vibrational pattern of these carbon nanostructures. The Raman response of  $^{13}\text{C}_{60}$  after encapsulation in fullerene peapods differs from that of isotope-natural species,  $^{\text{Nat}}\text{C}_{60}$ . The Raman  $\text{A}_g(2)$  mode of encapsulated  $^{13}\text{C}_{60}$  is up-shifted in

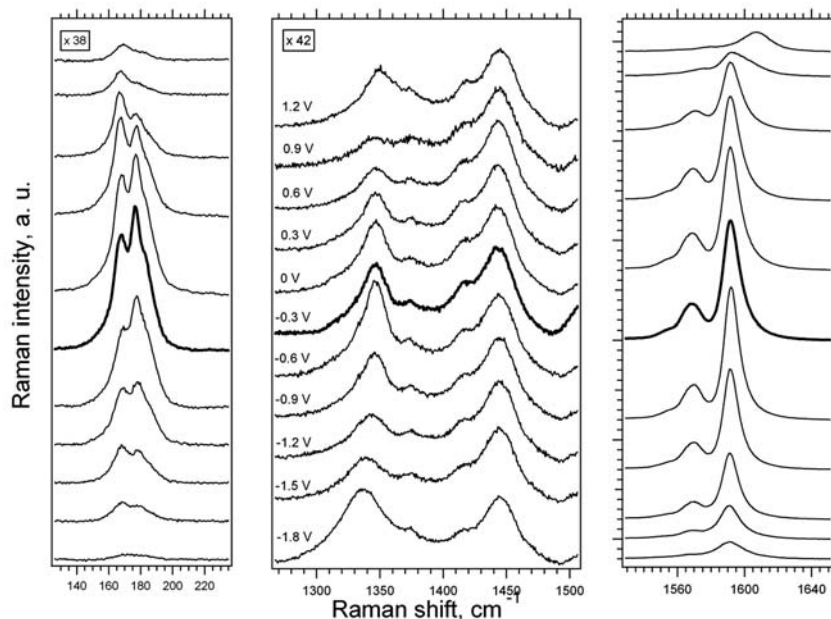


Fig.: Raman response of  $^{\text{Nat}}\text{C}_1$ -DWCNTs,  $^{13}\text{C}_1$ -DWCNTs and SWCNTs (from top to bottom). The spectra were measured on dry buckypaper. Intensities of spectra were normalized using the F1g line of Si at  $520.2\text{ cm}^{-1}$ . The excitation energy was  $1.83\text{ eV}$ . Spectra were offset for clarity but the intensity scales are identical in the respective window.

frequency compared to that in  $^{13}\text{C}_{60}$  peapods with the same filling factor. The chemical doping of  $^{13}\text{C}_{60}$  peapods with K-vapor leads to the downshift of  $A_g(2)$  mode similarly as in case of  $^{13}\text{C}_{60}$  peapods. The  $^{13}\text{C}_{60}$  peapods were successfully transformed into DWCNTs, which confirms high filling of SWCNT with  $^{13}\text{C}_{60}$ . The DWCNTs exhibited distinctly downshifted G and D Raman modes for inner tubes, which confirms that only inner tubes were enriched by  $^{13}\text{C}$ . The in situ Raman spectroelectrochemistry of  $^{13}\text{C}_{60}$  exhibits strong anodic enhancement, while for  $^{13}\text{C}_{60}$  peapods the enhancement is weak only. On the other hand, the electrochemical charging of the inner-tube labeled double walled carbon nanotubes  $^{13}\text{C}_i$ -DWCNTs followed the behavior of ordinary  $^{13}\text{C}_i$ -DWCNTs as indicated by in situ Raman spectroelectrochemistry. In addition we follow the spectroelectrochemical behavior of the G mode of inner tubes in  $^{13}\text{C}_i$ -DWCNTs from the start of the doping, which was not possible for  $^{13}\text{C}_i$ -DWCNTs.

**Cooperation** J. Heyrovsky Institute of Physical Chemistry, AVCR, Prag, CZ  
**Funded by** DFG

### Magnetic ground state in molecular complex with all-AFM couplings

C. Golze, V. Kataev, B. Büchner, S. Khanra, P. Chaudhuri

Single-molecule magnets (SMM) are nanosize multinuclear magnetic molecules with a finite total spin  $S$  in the ground state and an axial magnetic anisotropy,  $D < 0$ . The objective of the synthesis of these molecules is to increase the potential well  $|D|S^2$  which is separating the degenerate spin orientations  $|S, S_z = -S\rangle$  and  $|S, S_z = +S\rangle$  and is therefore allowing for data storage. Obviously, for a homonuclear core the highest possible ground state spin can be achieved only by all-ferromagnetic (FM) intra-molecular interactions. In this work we present a newly synthesized molecule with a magnetic core adopting the much more favored antiferromagnetic (AFM) exchange. Here, the strategy of getting a highly magnetic core is to compose it of *heterometallic* ions  $\text{Fe}^{3+}$  and  $\text{Cu}^{2+}$ : since the iron spin is  $5/2$  and copper is only  $1/2$ , the net spin of AFM coupled Fe-Cu pairs is 2. Fig. a) shows the core structure of the investigated tetranuclear  $\text{Fe}_2\text{Cu}_2$  complex with butterfly motif. The irons on the wing-tips are AFM coupled to the Cu of the butterfly's body either by a hydroxo- and an oximato-bridge,  $J_1 \sim 100$  K, or by a single oximato-bridge,  $J_2 \sim 10$  K. The exchange between the two Cu ions of the body is mediated by the Cl and is weakly AFM,  $J_3 \sim 1$  K. The resulting coupling scheme in Fig. a) shows the two Fe spins aligned parallel, while the Cu spins are antiparallel with respect to them. Measurement of the pulse-field magnetization at 4 K indeed confirms the depicted coupling scheme:  $M(H)$  exhibits a saturation plateau of  $8 \mu_B$ /molecule for fields  $H > 10$  T which is a clear indication for an  $S = 4$  ground state.

Furthermore, high frequency electron spin resonance (ESR) was measured on the compound. The temperature dependence of the powder spectrum is shown in Fig. b). The broad signal at 2 K is due to the strongly polarized magnetic ground state,  $|S, S_z = -S\rangle$ , where the spectrum comprises unresolved fine-structure due to additional intra-multiplet spin-flips within the  $S = 4$  state. At high  $T$  a single Lorentzian absorption line evolves due to ESR in excited multiplets. The resonance branches in Fig. c) exhibit a linear  $\nu(H_\nu)$  dependence of the fine structure in the spectrum (indicated by arrows in Fig. b)). Extrapolation of  $\nu(H_\nu)$  to  $H = 0$  gives a direct estimate of a magnetic anisotropy gap  $\Delta \sim 1.7$  K which suggests a substantial single molecule magnetic anisotropy. Therefore, the novel  $\text{Fe}_2\text{Cu}_2$  - complex appears to be a possible candidate for an all-AFM coupled SMM.

**Cooperation** MPI for Bioinorganic Chemistry, Mülheim  
**Funded by** DFG

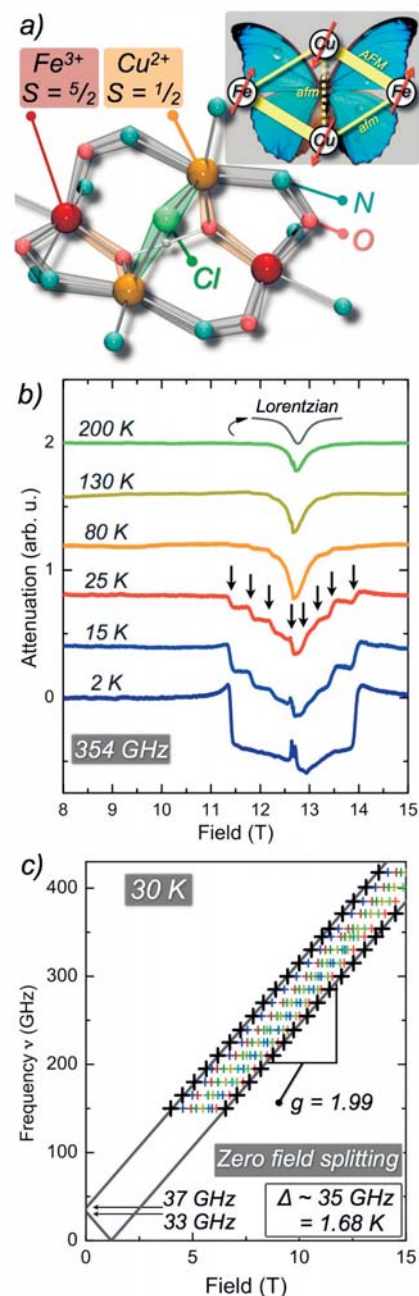


**Fig.:** a) Butterfly core structure of the  $\text{Fe}_2\text{Cu}_2$  molecule. Fe-Cu bondings are either strongly or moderately AFM, Cu-Cu interaction is very weakly AFM. b) ESR temperature dependence: The evolving fine-structure in the domain 2 - 25 K is due to resonance absorption in the lowest lying  $S = 4$  multiplet. For  $T > 100$  K temperature activated (excited) multiplets are detected. c) The resonance branches exhibit a linear behavior according to the  $g$ -factor of  $g = 1.99$ . Extrapolation to  $H = 0$  suggests an appreciable zero-field splitting  $\Delta$  of the order of 1.7 K.

## Determination of trap distributions from current characteristics of pentacene field-effect transistors with surface modified gate oxide

S. Scheinert (1), K. P. Pernstich (2), B. Batlogg (2), G. Paasch

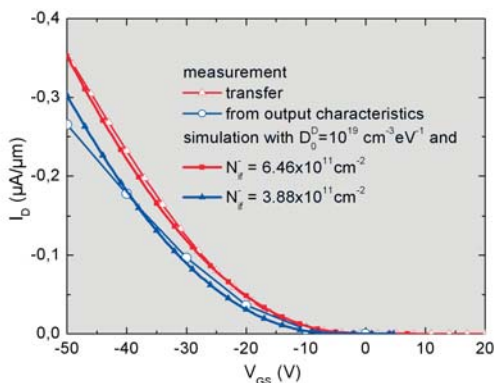


**Fig.:** Transfer characteristics (directly measured and extracted from the output characteristics) of one device for  $V_{DS} = -50$  V in comparison with the simulated curves with a mobility of  $0.85$   $\text{cm}^2/\text{V}$  s including exponentially distributed donorlike bulk traps with a maximum density of states of  $10^{19}$   $\text{cm}^{-3}$   $\text{eV}^{-1}$  lying  $0.2$  eV above the valence band, a decay constant of  $0.1$  eV, and fixed negative interface charges  $Q_{if} = eN_{if}$  as indicated in the legend.

Organosilanes with different functional groups forming a self-assembled monolayer (SAM) on the gate oxide of organic field-effect transistors (OFET) are frequently used to enhance the mobility and hence the OFET performance. It has been demonstrated [1], that in addition a controllable shift of the threshold voltage is caused by the SAM in pentacene thin film transistors. The observed broadening of the subthreshold region indicates that the SAM creates additional trap states. Indeed, it is well known that traps strongly influence the behavior of OFETs. Therefore, the so-called “amorphous silicon model” has been suggested to be appropriate to describe OFETs. The main specifics of this model are transport of carriers above a mobility edge obeying Boltzmann statistics and exponentially distributed tail states and deep trap states. Here [2], approximate trap distributions are determined by adjusting two-dimensional numerical simulations to the experimental data. It follows from a systematic variation of parameters describing the trap distributions that the existence of both donorlike and acceptorlike trap distributions near the valence band, respectively, and a fixed negative interface charge have to be assumed. For two typical devices with different organosilanes the electrical characteristics can be described well with a donorlike bulk trap distribution, an acceptorlike interface distribution, and/or a fixed negative interface charge (see Fig. 1). As expected, the density of the fixed or trapped interface charge depends strongly on the surface treatment of the dielectric. There are some limitations in determining the trap distributions caused by either slow time-dependent processes resulting in differences between transfer and output characteristics (Fig. 1), or in the uncertainty of the effective mobility.

[1] K. P. Pernstich et al. *J. Appl. Phys.* **96**, 6431 (2004).

[2] S. Scheinert et al. *J. Appl. Phys.* **102**, 104503 (2007)

Cooperation TU Ilmenau (1), ETH Zürich (2)

Funded by DFG, Swiss BBW as part of EUROFET

## Electrical percolation of tailored CNT in polymer composites

M. Ritschel, A. Leonhardt, C. Täschner, S. Oswald, W. Gruner, B. Krause (1), P. Pötschke (1)

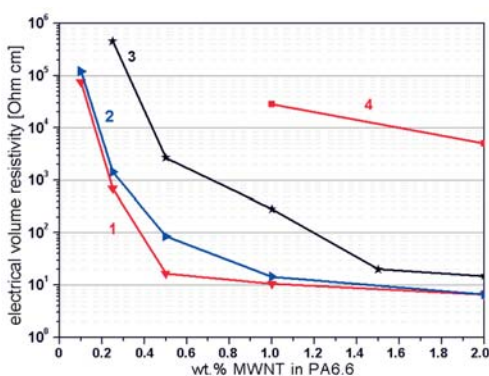


**Fig.:** Electrical volume resistivity of PA 6.6 filled with different CNTs in dependence on filler content: 1...aerosol CVD (acetonitrile) – CNTs; 2...aerosol CVD (cyclohexane) – CNTs; 3...commercial CNTs; 4...fixed bed CVD - CNTs.

Composite materials based on CNTs and insulating polymers are potential candidates for electrostatic dissipative or conductive applications. The structure and properties of the embedded CNTs strongly determine the electrical conductivity of the composites. Therefore the synthesis of CNTs with a high crystalline perfection of the outer C-shells and a narrow diameter distribution is absolutely essential. By using two different CVD methods, the fixed bed and the aerosol technology, we have synthesised such tailored CNTs. With the fixed bed CVD in dependence on the composition of used solid catalyst (Fe/Mo/MgO) various types (SW, DW, or MW) of CNTs or mixtures of them can be produced, whereas the aerosol CVD delivers MWCNTs with a narrow diameter distribution ( $\sim 20$  nm).

We have embedded these different types of CNTs (and additionally a commercial product) in polyamide 6.6 and determined the electrical volume resistivity of these composites. Concerning the percolation behaviour the aerosol-CNTs show the lowest percolation concentration at  $0.1$  wt%, relatively independent of the used C-source (acetonitrile or cyclohexane). This percolation threshold is much lower than values measured and reported in the literature, so far (Fig.).

The aerosol-CNTs can be embedded into the polymer without chemical pre-treatment. Before further processes the fixed bed-CNTs must be purified by washing in acids to remove the catalyst material. This chemical treatment changes the surface of the CNTs via formation of functional groups such as OH and COOH and can be identified by XPS and chemical element analysis. The commercial and fixed bed-CNTs possess often amorphous C-deposits on the tube surface which decreases the electrical conductivity and therefore the percolation concentration increases.

The used aerosol-CVD delivers advantageously very pure CNTs with well developed crystalline C-shells and can be bottom-of-the-line upscaled for an industrial process.

**Cooperation** Leibniz-Institut für Polymerforschung Dresden (1)  
**Funded by** BMBF

### A Carbon-wrapped nanoscaled thermometer for in-vivo temperature control in biological environment

A. Wolter, A. Vyalikh, R. Klingeler, D. Haase, S. Hampel, A. Leonhardt, B. Büchner

One promising field of nanotechnology concerns the diagnostic and therapeutic usage of nanoparticles at the cellular level. An example is the nanoscaled thermometer based on NMR-active material encapsulated in carbon nanotubes. Here, strongly temperature dependent NMR parameters of the filling are exploited for spectroscopic in-situ temperature control. Since many alkali and cuprous halides are known to show pronounced temperature dependencies of NMR parameters, two members of the family of cuprous halides (CuI, CuBr) have been chosen as first filling agents.

The NMR frequency data for both halide nuclei exhibit a linear temperature dependence which is explained by lattice effects including both lattice vibration and lattice expansion. But the relative small slope of this linear function leads to an error of  $\geq 15$  K and is therefore not sufficient for an accurate temperature control. However, for both  $^{127}\text{I}$  and  $^{81}\text{Br}$  nuclei the temperature dependence of the spin-lattice relaxation rate ( $T_1^{-1}$ ) is found to be in very good agreement with the law  $T_1^{-1} \propto T^2$  that is expected for a Raman two-phonon quadrupolar process. From the mean squared errors of the fitting coefficients an estimate of the temperature accuracy can be achieved yielding a value of 2 K for the  $^{127}\text{I}$  signal in the temperature range of biological interest (i.e. 290–320 K). This is a promising result and a good starting point to look for further filling materials of CNT in order to increase the accuracy of temperature determination.

**Cooperations** TU Dresden, Szczecin Univ. of Technology  
**Funded by** DFG, EU (Marie-Curie RTN CARBIO)

### Copper-filled Carbon Nanotubes

D. Haase, S. Hampel, A. Leonhardt, J. Thomas, N. Mattern, B. Büchner

Since Carbon Nanotubes (CNT) represent hollow, cylindrical nanostructures they provide excellent templates for the fabrication of carbon wrapped nanocables. Thus the filling material can be protected against chemical and physical alteration by the stable carbon shell. Filled nanotubes might be used as challenging devices at the nanoscale such as nanoelectric circuits, nanocables, nanopipettes or nanothermometers. Among all metals copper exhibits the highest electrical and thermal conductivity apart from silver. Despite that it shows a low binding energy towards carbon (about 0.1 eV). Due to these qualities it is recommended to be a suitable material for applications as mentioned above.

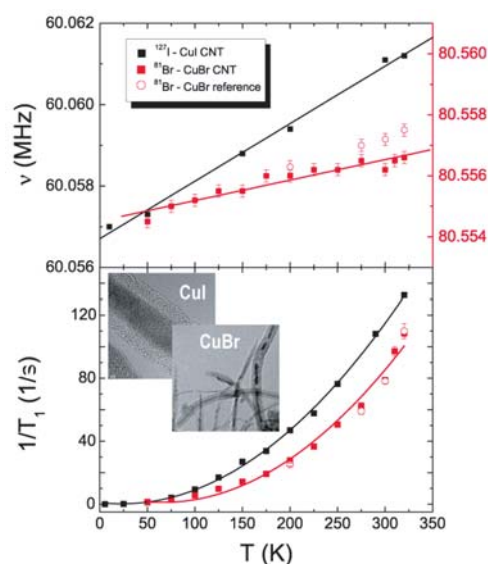


**Fig.:** Temperature Dependencies of  $^{127}\text{I}$ , and  $^{81}\text{Br}$  nuclear magnetic resonance parameters measured for cuprous-halide filled carbon nanotubes as well as for  $^{81}\text{Br}$  from a reference powder CuBr. All NMR measurements were performed on powder material in an external magnetic field of 7.05 T. (a) Nuclear magnetic resonance frequency. (b) Nuclear spin-lattice relaxation rate; inset shows TEM images of CuI- and CuBr-filled carbon nanotubes after synthesis.

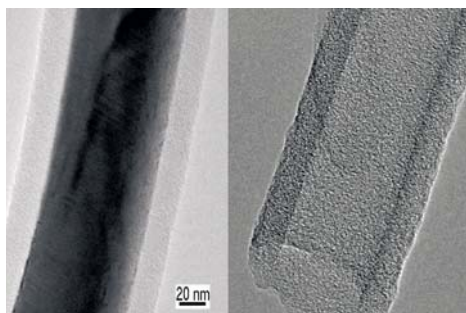


**Fig.:** left: as grown Copper-filled Carbon Nanotube right: empty amorphous Carbon Nanotube remaining after thermal treatment.

Compared to the synthesis of *in situ* copper filled CNT by arc discharge or CVD methods we present a simple one step route in which the pyrolysis of the metal-organic precursor Copper(II)-acetylacetonate results in the growth of carbon wrapped copper nanowires under certain conditions. These nanowires consist of a single crystalline copper core encased by amorphous carbon. A thermal aftertreatment near the melting point of Cu melts the filling and thus leads to the formation of empty amorphous carbon nanotubes with spherical Cu particles attached to the end. Due to the nanoscale dimension of the products a decrease in melting point can be observed. It has been proven that the Cu core melts already at a temperature of 800 °C. This process is of great importance, e. g. for the application of such nanostructures as nanopipettes or nanocables which has already been demonstrated by Golberg et al. The nanowires have been probed electrically and then manipulated inside a high-resolution transmission electron microscope using a piezo-driven STM-TEM stage.

**Cooperation** Nanoscale Materials Center, National Institute for Materials Science, Tsukuba Japan

### Magnetic force microscopy sensors using filled carbon nanotubes

T. Mühl, F. Wolny, U. Weißker, A. Leonhardt, B. Büchner

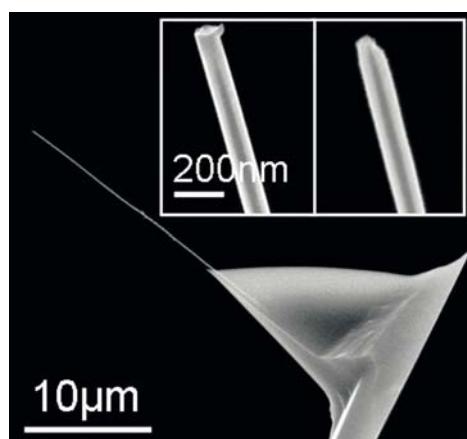


**Fig.:** Iron-filled carbon nanotube attached to a cantilever probe. Insets: free end of the nanotube before (center) and after (right) electron beam assisted local oxidation.

There are several approaches to image magnetization or stray-field structures such as spin-polarized STM, Kerr microscopy, SEM with polarization analysis, magnetic exchange force microscopy, resonance force microscopy, and magnetic force microscopy (MFM). The latter represents a stray-field imaging method which combines high spatial resolution in the 10 nm range with low sample preparation requirements.

In our approach MFM sensors are prepared by pinning iron-filled carbon nanotubes to conventional cantilever probes using mechanical nanomanipulation techniques. In addition, electron beam assisted local oxidation has been applied to remove empty parts of the nanotubes. The nanotube MFM sensor shown in the figure did not allow efficient sample-probe interactions due to the empty part of the nanotube (central figure inset). This empty part has been removed by applying a 10 keV electron beam in a 20 Pa water atmosphere (right inset). After this treatment the nanotube sensor reveals dramatically increased sensitivity and spatial stray-field resolution.

The filled carbon nanotubes used in this study were prepared by thermal CVD with ferrocene being the only carbon and iron source. Since nanotubes tend to grow aligned when high heating rates are used, during the CVD process the reactor temperature was increased from 300 °C to 900 °C using a heating rate of 1 K/s.

**Cooperation** Ohio State Univ., USA

**Funded by** DFG

### Leibniz Pact project on nanoscaled magnets: Structure and electronic properties of Li-doped vanadium oxide nanotubes

I. Hellmann, A. Popa, Y. Arango, E. Vavilova, R. Klingeler, V. Kataev, Ch. Täschner, A. Leonhardt, M. Knupfer, B. Büchner

Vanadium oxide nanotubes (VO<sub>x</sub>-NTs) are considered to be promising candidates for applications upon functionalization by intercalation or doping. The idea is to tune the vanadium valence in a low-dimensional environment and to switch the properties of these nanotubes. We indeed observe that a superparamagnetic response evolves in VO<sub>x</sub>-NTs upon doping with lithium.

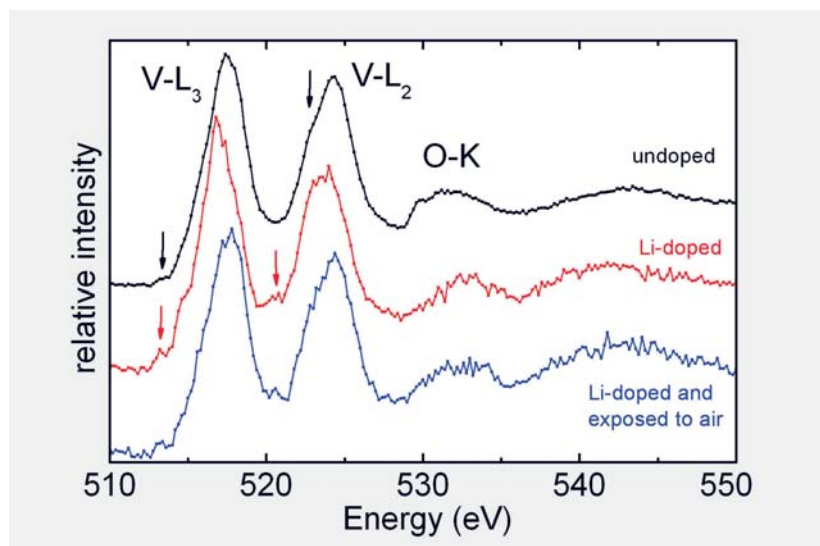


**Fig.:** Core level excitation spectra of VO<sub>x</sub>-NTs. Upon introducing electrons by doping with lithium, the position and the shape of the V L-edges as well as the O K-edge change. The characteristics of the undoped material are partly restored when the sample is exposed to ambient conditions. The curves were normalized at 550 eV and are vertically displaced for comparison.

The influence of Li-doping on the mixed-valent vanadium oxide nanotubes has also been investigated using electron energy-loss spectroscopy (EELS). Particularly, we have turned our attention to the spectral features arising from the V 2p core levels, the so-called V L-edges. Simultaneously obtained electron diffraction profiles shed light on the structural stability upon Li addition. Both, the diffraction data and the vanadium L-edges show that a reversible insertion of lithium can be achieved to a large extent. The VO<sub>x</sub>-NT's layer structure is stable during addition and removal of electrons provided by lithium, but the vanadium valence is tuned. We estimate a possible charge transfer to vanadium by Li-doping of approximately 1.5 electrons with an uncertainty of about 15 - 20 %.

**Cooperation** Kazan Physical Technical Institute, RAS, Kazan, Russia; Institute of Solid State Chemistry, Russian Academy of Science, Yekaterinburg; Laboratoire de Réactivité et de Chimie des Solides, Univ. de Picardie J. Verne, Amiens, France  
**Funded by** DFG (KL 1824/2), Leibniz Pact 2007

## Research Area 4 Metastable alloys

### Synchrotron X-ray analysis of solidification processes in $\gamma$ -TiAl turbine blade alloys

O. Shuleshova, H.-G. Lindenkreuz, N. Mattern, W. Löser, B. Büchner

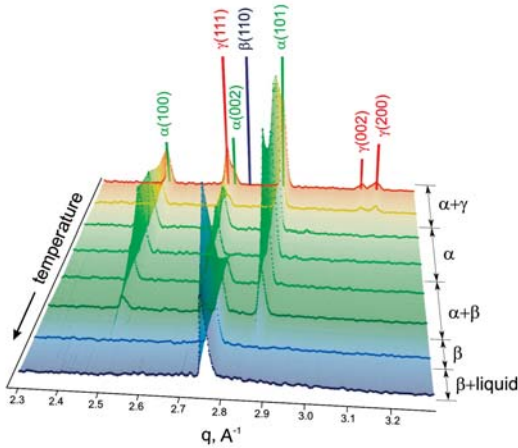


**Fig.:** X-ray diffraction patterns as function of temperature from *in situ* synchrotron X-ray analysis of the Ti-46Al-8Nb alloy. The constituent phases  $\beta$ -Ti,  $\alpha$ -Ti and  $\gamma$ -TiAl are indexed and inferred phase fields are specified.

A unique containerless method for *in situ* phase analysis of electromagnetically levitated droplets has been applied in joint experiments with DLRZ at ESRF Grenoble for *in situ* synchrotron X-ray analysis of ternary  $\gamma$ -TiAl turbine blade alloys. This was the first definite experimental identification of  $\beta$ -Ti type primary solidification of the Ti-46 at%Al-8 at.%Nb alloy (Fig.). This finding and the study of related alloy compositions enabled a clarification of existing conflicting Ti-Al-Nb phase diagrams. The experiments provide valuable new data for a reassessment of the Ti-Al-Nb phase diagram. We unambiguously prove that by Nb addition the  $\beta$ -Ti primary solidification range extends to higher Al contents. Moreover, the determination of phase transformation sequences in the high temperature range is important for designing microstructures of commercial turbine blade materials. The method offers a great potential for phase diagram analyses of alloys containing refractory metals and intermetallics.

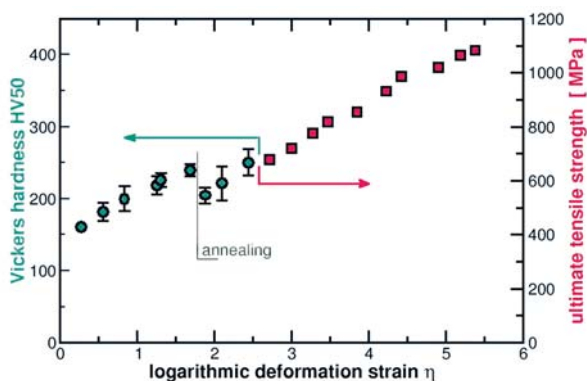
**Cooperation** Deutsches Zentrum für Luft- und Raumfahrt (DLRZ) Köln, ESRF Grenoble  
**Funded by** EU

### Highly strengthened conductor materials

J. Freudenberger, J. Lyubimova, H. Klaus and L. Schultz

The strain of heavily cold worked Cu-7m%Ag-0.05m%Zr conductor materials has been further enhanced by means of recovery, recrystallisation and grain growth processes. The as drawn materials exhibit an inhomogeneous structure with elongated grains (grain size about 100 nm). The large deformation strain of  $\eta=4.3$  that has been applied causes a subgrain structure accompanied by a high dislocation density. The key issue to adjust the microstructure of the alloy is represented by an optimization of the thermo-mechanical treatment. The initial heat treatments cause (i) the formation of a solid solution and (ii) the precipitation reaction. The alloys were investigated by means of mechanical, electrical and microstructural analyses. Heat treatments are shown to be an effective tool to enhance the strain to failure. If applied between several deformation steps the heat treatment causes an increase of both, strain and strength. The fatigue performance of the Cu-Ag alloys proved to fit the prospected service requirements in that a fatigue lifetime in the range of 5 - 9000 cycles to failure is observed, when a stress amplitude of  $\sigma_a = 500$  MPa at a load ratio  $R = 0.1$  is applied.

**Fig.:** Dependence of the Vickers hardness HV50 as well as the ultimate tensile strength of Cu-7m%Ag-0.05m%Zr on the logarithmic deformation strain. The kink at about  $\eta=1.7$  arises from intermediate heat treatments at 850°C/5h + 400°C/18h.



In Addition tapes have been cold rolled from Cu-Ag conductor materials. An ultimate tensile strength of 1.1 GPa is observed after a cold deformation strain of  $\eta = 5.4$  was applied. These are promising candidates for miniaturized plug contacts or conductive highly strengthened substrates.

**Cooperation** Forschungszentrum Dresden-Rossendorf, Univ. of Oxford, LNCMP Toulouse, Univ. of Poitiers, HMFL Nijmegen.

**Funded by** DFG FR 1714/2-1

### **Phase Stability of Competing Structural Motifs in Bimetallic Nanoparticles**

D. Pohl, E. Mohn, B. Rellinghaus, L. Schultz

Owing to their nanoscopic size and an enhanced surface-to-volume ratio the thermodynamic equilibrium structure and morphology of nanoparticulate materials may significantly deviate from its bulk counterparts. E.g., in stoichiometric bimetallic FePt and CuAu nanoparticles, the low surface free energy of  $\{111\}$  facets results in the energetic preference of (multiply) twinned structures which compete with the chemically ordered, tetragonal  $L1_0$  phase – the thermodynamic ground state of bulk FePt and CuAu at room temperature. A comparative investigation of the occurrence of structural motifs in gas-phase prepared FePt and CuAu nanoparticles has revealed that owing to a reduced twin boundary energy, the occurrence of (multiply) twinned particles is more frequent in CuAu particles as compared to FePt. In addition, thermal annealing results in a faster and more effective inter-particle sintering in CuAu. Since nanoparticle coalescence is known to occur predominantly via surface diffusion [1], this is attributed to the lower activation energy for surface diffusion in CuAu than in FePt. Whereas in FePt nanoparticles the (partial) formation of the  $L1_0$  order is observed, the ordering in CuAu particles is found to be suppressed owing to both the stronger energetic competition of twinned structures and the slower ordering kinetics in CuAu which exhibits a significantly lower (bulk)  $L1_0$  ordering temperature. Ion irradiation of  $L1_0$  ordered FePt nanoparticles was found to result in disordering and a preferred transformation to A1 type (fcc) single crystal particles independent of the ion energies (0.5 keV – 40 keV He<sup>+</sup>). It is shown that ion irradiation also leads to a de-twinning of both FePt and CuAu particles. Molecular dynamics studies on the effect of ion irradiation on CuAu particles reveal that both the disordering and the de-twinning are caused by a metastable amorphisation upon the ion irradiation.

[1] S. Tsyganov et al. Phys. Rev. B 75 (2007) 045421

**Cooperations** FZ Dresden-Rossendorf, Univ. of Technology Darmstadt, Univ. Duisburg-Essen (SFB 445)

### **Corrosion and Hydrogen Reactivity of multicomponent Mg-based alloys**

A. Gebert, A. Teresiak, V. Hähnel, V. Bunea, M. Uhlemann, J. Thomas, J. Eckert, L. Schultz

The corrosion behaviour of the  $Mg_{65}Cu_{7.5}Ni_{7.5}Ag_5Zn_5Gd_5Y_5$  bulk metallic glass was studied. A superior resistance and passivation ability compared to that of Mg and the conventional AZ31 alloy was detected in weakly acidic to strongly alkaline solutions. This is attributed to a beneficial effect of the alloying components, which are homogeneously mixed in the amorphous phase. They cause the establishment of a more noble alloy state and possess a higher tendency for surface passivation than the main component Mg.

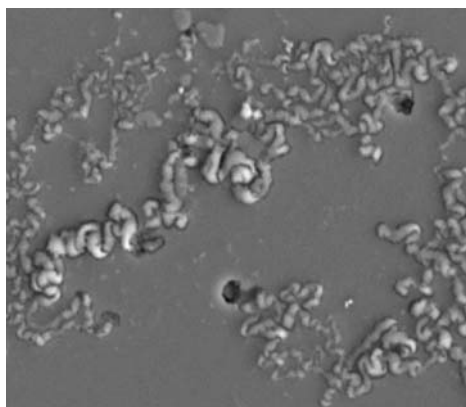


**Fig.:** Filiform corrosion on passivated  $Mg_{65}Cu_{7.5}Ni_{7.5}Ag_5Zn_5Gd_5Y_5$  bulk metallic glass surface.

A high sensibility to chloride-induced corrosion exists, which is at low chloride concentrations strongly pH value dependent. Filiform corrosion occurs with filaments propagating randomly on the passivated amorphous surface (Fig.). Y-rich crystalline defects in the bulk glassy sample have no evident effect on the corrosion processes.

Currently, Mg–Ni–RE alloys attract great interest as new materials for low temperature hydrogen charging. The recently discovered  $Mg_2NiLaH_7$  hydride shows with 2.8 wt% (109 g/l H) a much higher hydrogen content than the well-known  $LaNi_5H_x$ - (1.5 wt.%) and  $TiV_2H_x$ - (1.7 wt.%) alloys. We investigated the formation of the complex hydride  $Mg_2NiLa(Co)H_{7\pm x}$  by using various process routes, which aim at achieving material with nanocrystalline microstructure. The  $Mg_2NiLaH_7$  forms completely by intensive ball milling of an inductively molten master alloy of Mg<sub>2</sub>NiLa under hydrogen for 7.5h. Also, the gradual electrolytic charging of the master alloy using a current density of  $-1mA/cm^2$  succeeded in forming the hydride. Starting from melt-spun amorphous ribbons, the crystallisation to nanocrystalline  $Mg_2NiLa$  and a subsequent hydrogenation under 0.5MPa hydrogen for 26h were performed and monitored by means of *in situ* high temperature XRD. A partial substitution of Ni by 5 at.% Co in the  $Mg_2NiLa$  phase leads to a larger unit cell volume due to the larger atomic radius of Co compared to Ni and reduces the reaction time of the hydride formation by intensive ball milling drastically.

**Cooperations** Yonsei Univ. Seoul, Korea; Politehnica Bucharest, Romania; Univ. of Sofia, Bulgaria; TU Dresden

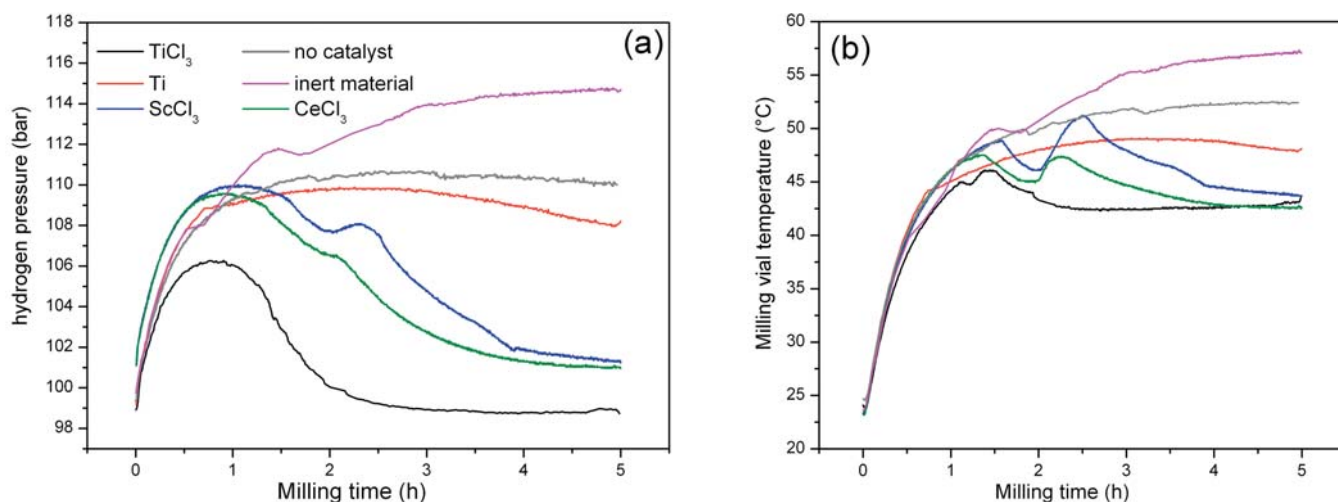
### New Hydrides

O. Gutfleisch, C. Rongeat, I. Llamas-Jansa, B. Gebel, M. Herrich, L. Dunsch, S. Oswald, A. Teresiak, M. Uhlemann, A. Gebert, L. Schultz

Human development has caused a depletion of natural energy resources and climate changes with non-predictable consequences. New energy concepts are required for the future of our industrial society. The only known energy carrier with a high energy density and no emission of greenhouse gas is hydrogen.

Research of solid-state storage of hydrogen - for e.g. zero-emission vehicle propulsion and other mobile applications - is pursued by exploring functional complex hydrides such as alanates, borohydrides and nitride based amides and imides. These materials offer several advantages over conventional metal hydrides (e.g.  $MgH_2$ ), provided one or more of the following limitations: a) unfavourable thermodynamics (high temperatures to release hydrogen), b) poor kinetics (low rates of hydrogen release and

**Fig.:** Evolution of a) hydrogen pressure and b) temperature during high pressure reactive milling of NaH + Al + 4% mol of different catalyst (pure Al and NaH + Al were also milled with the same conditions for comparison). Starting pressure is 100 bar, changes are monitored in-situ using an "intelligent" milling vial from *evico-magnetics*.



uptake), c) decomposition pathways involving the release of undesirable by-products (e.g. ammonia), and/or d) an inability to reabsorb hydrogen at modest temperatures and pressures (i.e. “irreversibility”) can be overcome.

Our work includes the thermodynamic and kinetic characterisation with high-pressure differential scanning calorimetry, gravimetric and pressure-composition-temperature analysis as well as the study of hydrogen dynamics using in-situ XPS, XRD and Raman in order to understand details of the complex sequence of transformations, to identify intermediate reaction products and rate determining steps in complex hydrides and reactive hydride composites. Novel processing techniques such as high hydrogen pressure reactive milling - giving immediate feed-back about catalyst efficiency already during synthesis (see figure) - are used in order to identify new materials with high reversible hydrogen contents.

**Cooperation** EMPA, Switzerland, GKSS Research Centre Geesthacht, FZ Karlsruhe, Univ. of Amsterdam, Netherlands, Institute for Energy Technology Oslo, Norway, Univ. of Birmingham, UK, Univ. of Rome “La Sapienza”, Italy  
**Funded by** EU IP (NESSHY), HGF (FuncHy), EU RTN (COSY)

### Fatigue of $\text{LiCrMnO}_4$ cathodes in Li-ion batteries

K. Nikolowski, A. Voss, N. N. Bramnik, H. Ehrenberg, J. Eckert

Doped-spinels of general formula  $\text{LiM}_x\text{Mn}_{2-x}\text{O}_4$  are promising candidates for cathodes in Li-ion batteries with cell voltages close to 5 V vs.  $\text{Li}/\text{Li}^+$ . Their application in hybrid electric vehicles (HEVs) is impeded mainly by insufficient lifetime and cycle stability. Fatigue in the title compound with  $M=\text{Cr}$  and  $x=1$  was investigated in the frame of the new research topic 4.5.1 on degradation phenomena and working principles in Li-ion battery materials [1]. A two-step process during Li-extraction is indicated by two peaks at 4.84 V (2) and 4.94 V (3) in the incremental capacities, determined by the potentiostatic intermittent titration technique (PITT). Note that peak (1) is due to the oxidation of residual  $\text{Mn}^{+III}$  to  $\text{Mn}^{+IV}$  because of some Mn-excess,  $\text{Mn}:\text{Cr}=1.08(1):0.92(1)$ , as detected by ICP-OES. The capacity fading with number of charge and discharge cycles depends strongly on the end-of-charge voltage and reveals a pronounced correlation between fatigue and an electronic reconfiguration accompanied with the second oxidative peak (3). A partial charge transfer between  $\text{Mn}^{+IV}/\text{Cr}^{+IV}$  and  $\text{Mn}^{+III}/\text{Cr}^{+VI}$  is proposed to explain the rapid degradation in the highly charged state by the structural Jahn-Teller distortion occurring for the  $\text{Mn}^{+III}$  state. Such a mechanism would point out a strategy to an improved material by preventing the formation of  $\text{Mn}^{+III}$  during charging by appropriate dopants.

[1] K. Nikolowski et al. in press. DOI 10.1007/s11581-007-0177-9.

**Cooperation** TU Darmstadt, Hamburger Synchrotronstrahlungslabor am DESY  
**Funded by** DFG, SFB 595 and PAK 177

### Runner materials for winter sports

J. Eickemeyer, C. Rodig, D. Seifert, T. Wolf, M. Frey, H.-P. Trinks, S. Neumann, M. Schubert, A. Güth, R. Kunze, O. Gutfleisch, J. Freudenberger, L. Schultz

In recent years the nickel superalloy <040>, which is successfully used in sledge racing, was further developed in order to enable its application in speed skating. It was shown that a specific microstructure, which is attained by a nano-particle hardening mechanism, results in a high strength and high toughness material.

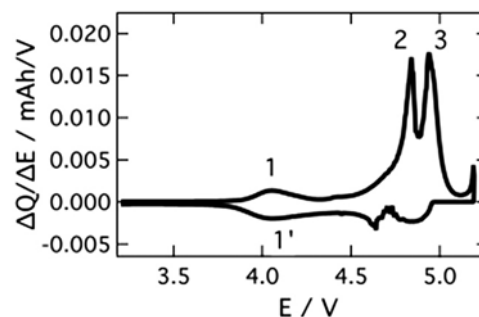


Fig. 1: Incremental capacity ( $\Delta Q/\Delta E$ ) versus cell voltage ( $E$ ) obtained from a PITT experiment with  $\Delta E=5$  mV and  $I_{\text{lim}}=C/20$ .

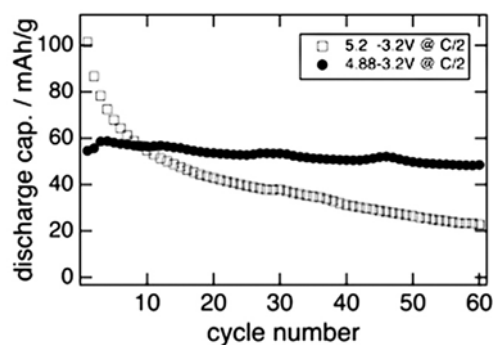


Fig. 2: Discharge capacity for cells charged to 4.88 V and 5.2 V, respectively.



**Fig.:** New skating blades made of nickel-based super-alloy <040S> embedded in a carbon fibre runner of the K2 speed skating shoe [made available by FES Berlin].

Although this specific runner material for speed skating <040S> was already successfully used at the Olympic Winter Games in Torino further evidence of its sliding potential under conditions of speed skating competitions was important. Therefore, the activities were focussed on proving the reliance of this material during speed skating including its wear resistance.

At the end of 2007 it can be assessed that the results obtained with <040S> runners confirmed the first positive impression from 2006. The <040S> runners contributed to set some new world records in ice skating sprint disciplines in 2007 and to several wins of World Cup races. Nevertheless, further optimisation of microstructure/properties is going on.

**Cooperation** FES Berlin, Fraunhofer- IKTS Dresden

### Multi-phase complex metallic alloys

S. Scudino, M. Sakaliyska, K.B. Surreddi, U. Kühn, M. Stoica, N. Mattern, H. Ehrenberg, J. Eckert

Within recent years, complex metallic alloys (CMAs) have been attracting much attention ranging from scientific curiosity about their complex structure to technological aspects of preparation and potential applications. Thanks to their peculiar structural characteristics, CMAs may become attractive candidates for structural applications. However, one major drawback for their use in engineering applications is the limited plastic deformability at room temperature. Grain refinement to nanometer regime together with the development of a heterogeneous microstructure combining nanostructured CMA particles with a ductile second-phase matrix can be employed to improve the room temperature ductility of CMAs.

Nanostructured single- or multi-phase materials can be prepared directly by solid state techniques, such as ball milling of CMAs precursors, or by controlled heat treatment of the milled powders. As a typical example, Fig. (a) displays the in-situ X-ray diffraction experiments as a function of temperature for the mechanically milled single-phase  $\beta$ - $\text{Al}_3\text{Mg}_2$ , revealing the formation of several nanocrystalline phases during heating. The ball milled powders can subsequently be consolidated by hot pressing, hot extrusion and spark plasma sintering to achieve dense nanostructured single- or multi-phase bulk specimens with properties that can be tuned within a wide range of size and volume fraction of the different phases.

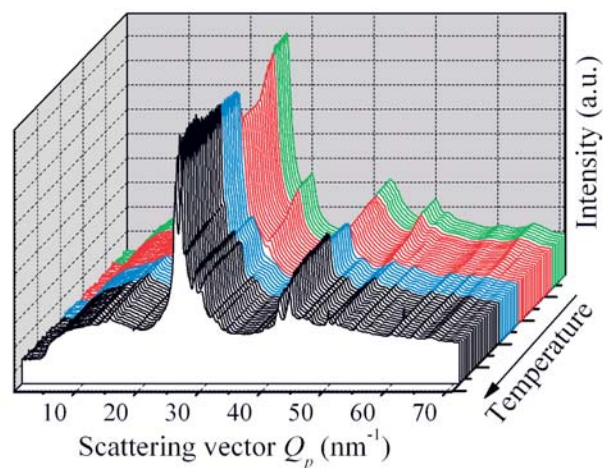


**Fig.:** In-situ X-ray diffraction patterns as a function of temperature for the mechanically milled single-phase  $\beta$ - $\text{Al}_3\text{Mg}_2$ .  
Green patterns: supersaturated  $\text{Al}(\text{Mg})$  solid solution (40 at.% Mg);  
red patterns: progressive rejection of Mg from the solid solution and formation of the  $\gamma$ - $\text{Al}_{12}\text{Mg}_{17}$  phase;  
blue patterns: metastable hexagonal  $\beta'$ - $\text{Al}_3\text{Mg}_2$ ;  
black patterns:  $\beta$ - $\text{Al}_3\text{Mg}_2$  (equilibrium phase).

**Cooperation** FZ Jülich; MPI Dresden; Univ. Frankfurt; Sejong Univ., Seoul/Korea; Univ. Torino, Italy; CNRS Grenoble, France

**Funded by** EU (NoE CMA)

## Research Area 5

### Thin film systems for electronics

#### Strongly coupled photonic molecules with embedded quantum dots

A. Rastelli, M. Benyoucef, S. Kiravittaya, Y. Mei, O.G. Schmidt

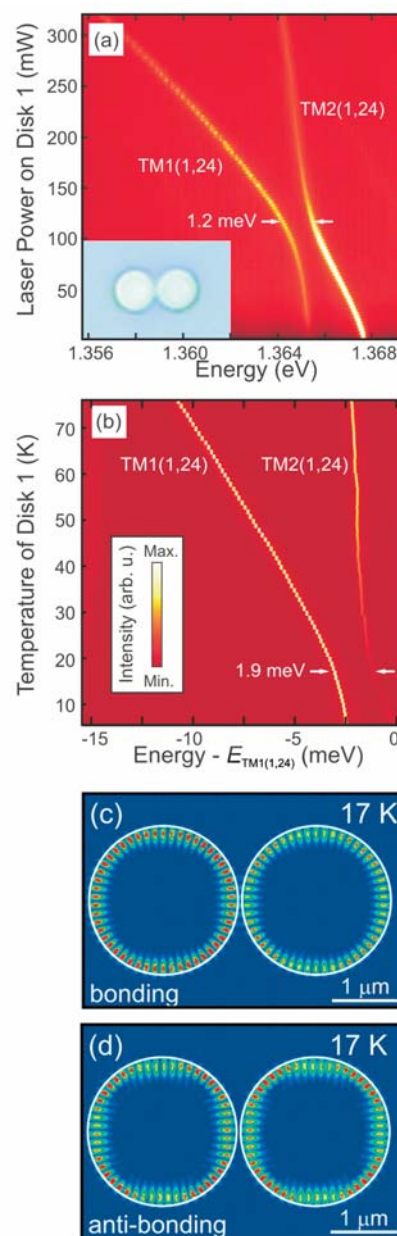
Coupled optical microcavities (photonic molecules) are attracting much interest for applications as delay lines in integrated photonic circuits and for solid-state quantum electrodynamics experiments.

We have studied with unprecedented detail the coupling between whispering gallery modes in two closely-spaced microdisk optical resonators made of GaAs. Self-assembled In(Ga)As quantum dots (QDs) were used as embedded light emitters and the mode positions were probed by micro-photoluminescence spectroscopy ( $\mu$ -PL). Because of fluctuations occurring during the fabrication process, nominally identical resonators show small structural differences, which result in a detuning of the optical modes. In order to compensate such differences and tune the modes of two disks into resonance, we have used the focused laser beam of our  $\mu$ -PL setup not only to probe the emission, but also to locally modulate the refractive index of one of the two disks by laser-induced heating.

This simple approach allowed us to smoothly scan the modes of one disk with respect to the modes of the other disk. When optical modes are brought into resonance clear anticrossing patterns are observed, indicating that the two disks are coupled and the eigenmodes of the system are spatially delocalized over the two resonators. Similar to real molecules, molecular-like optical modes can be classified as “bonding” and “anti-bonding” states, as supported by finite-difference time-domain (FDTD) simulations.

The method can be applied to other optical resonators and we envision the possibility of using molecular-like modes to achieve coherent excitation exchange between spatially separated two-level systems (QDs).

**Fig.:** (a) PL intensity map of two nearby microdisk resonators as a function of photon energy and laser power applied on one of the two disks (“Disk 1”). The modes of Disk 1 red-shift at higher rates with respect to the modes of Disk 2 because of local laser heating and consequent refractive index increase. Modes are assigned to transversal-magnetic modes (TM) according to calculations. Inset shows an optical microscopy image of the two disks with diameter of  $\sim 2.8 \mu\text{m}$ . (b) FDTD simulation of the mode position as a function of temperature of Disk 1. (c)-(d) Electric field profile of the molecular-like modes at the anticrossing point.



#### Advanced analytical glow discharges

V. Hoffmann, D. Klemm, M. Voronov, V. Efimova, K. Wetzig, J. Eckert

Instrumental improvements resulted in improved stability and reliability of GD-OES at depth profiling. Applying these improvements we were able to obtain reproducible information about concentration depth profiles in thin films. One example was the determination of impurities in 100 nm electrochemically deposited Copper layers. Even molecules, like monolayers of thiourea adsorbed on a copper surface were detected in dc mode, thus confirming rf measurements from Shimizu [1].

Due to the application of pulsed discharges new applications of glow discharges spectrometry (GDS) became possible in the recent years. Despite the reduced heat introduction into the sample, very high sensitivity is caused by huge currents within the first microseconds. Therefore it is possible to stretch the information of one monolayer by the application of about 200 pulses. Moreover, we could show that imaging of the light emitted from the plasma in optical GDS allows to obtain laterally resolved element distributions [2]. In the afterglow it is even possible to get molecular information about gaseous samples.

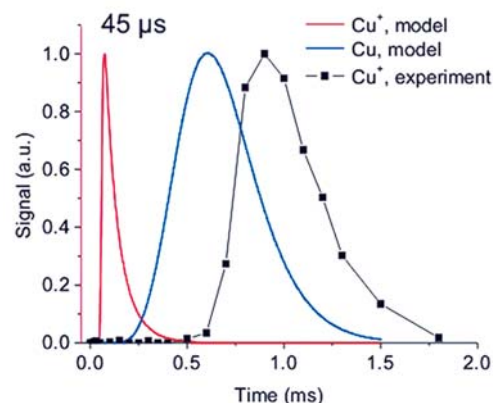


**Fig.:** Comparison between measured and calculated flow of Cu ions and atoms [3]

Fundamental investigations about the electrical characteristics of pulsed rf and dc discharges including plasma modelling resulted in more insight in the physical processes of GD. Especially, it became obviously, that there are secondary discharges existing in fast flow GD-MS, which has strong implication on further instrument development [3]. The evaluation of the voltage current curves gives access to gas temperature and density as input parameter for improved model calculations [4].

[1] K. Shimizu et al., JAAS, 2004, 19, 692

[2] M. Webb et al., Spectrochim.Acta B, 2006, 61, 1279

[3] M. Voronov et al., JAAS, 2007, 22, 1184

[4] L. Wilken et al., Spectrochim.Acta B, 2007, 62, 1085

Cooperation Indiana Univ., State Uni. of St. Petersburg, Spectruma Analytik GmbH Hof  
Funded by DFG, AiF, EU, Spectruma Analytik GmbH

### Magneto-electrodeposition of magnetic thin films

M. Uhlemann, J. Koza, X. Yang, K. Hennig, A. Gebert, L. Schultz, U. Wolff, C. Mickel

The effect of superimposed homogeneous magnetic fields up to 13 T with parallel and perpendicular orientation relative to the electrode surface on the electrochemical deposition of ferromagnetic alloys was investigated by means of potentiodynamic and potentiostatic methods and EQCM measurements in cells with different geometry. The change of the pH-value in front of the electrode is influenced by the applied field and affects significantly the morphology and magnetic properties of the deposited alloys. Smooth surfaces without defects and hydroxides were obtained in the parallel-to-electrode configuration. Interestingly, the spontaneous formation of hydroxides is also suppressed in magnetic fields perpendicular to the electrode. This behaviour is caused by a complex Lorentzforce driven convection as well as local induced field gradients. Modifications in the geometry affect the electrochemical behaviour clearly shown in the Fig. due to a changed convection which leads to deposits with different structural and physical properties. The deposition in alumina templates was carried out and analysed by XRD, MFM, TEM and discussed with respect to the applied magnetic field.

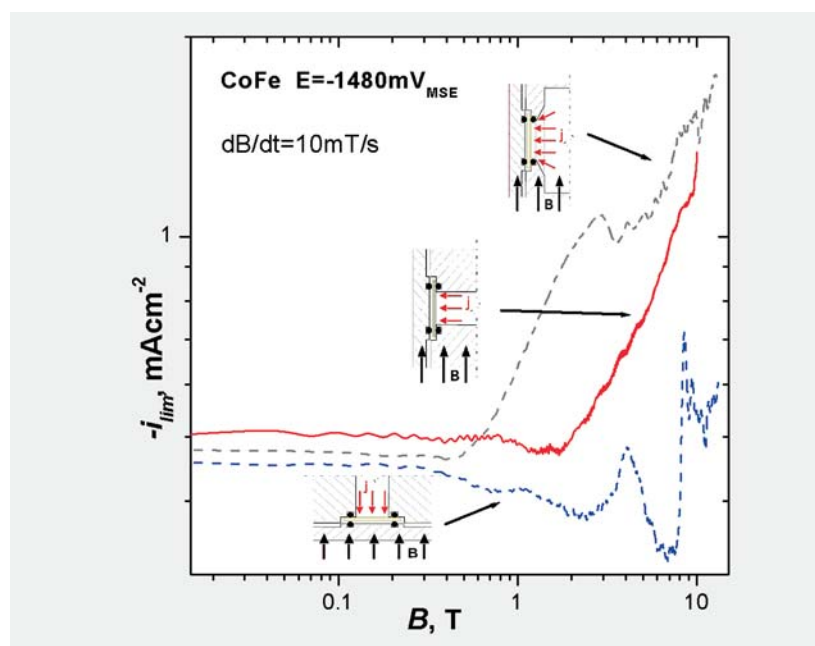


Fig.: Change of limiting current density for CoFe deposition in dependence on B for different cell configuration and magnetic field orientation.

The concentration profile in front of the electrode during deposition in applied inhomogeneous magnetic fields was studied time dependent with high resolution by a Mach-Zehnder interferometer and analysed by numerical calculation in cooperation with the TU Dresden and FZ Dresden-Rossendorf. Dependent on the direction of the applied field the buoyancy driven convection can be either suppressed or enhanced and shows interesting complex dynamics.

**Cooperation** TU Dresden, FZ Dresden-Rossendorf, Univ. Reims, High magnetic field laboratory, Grenoble, AGH Univ. of Science and Technology, Krakov  
**Funded by** DFG (SFB 609)

### Highly textured aluminium layers on piezoelectric substrates

S. Menzel, H. Wendrock, J. Thomas, T. Gemming

The effect of microstructure and, in particular, the texture of aluminium metallizations on stress or electromigration has been demonstrated some time ago. Hence, a performance improvement was also expected in ion beam sputtered Al films on different metal underlayers for application in surface acoustic wave (SAW) devices due to reduced acoustically induced stress migration effect (so called acoustomigration).

Aluminium thin films with thickness below 500 nm for application in high power SAW devices were prepared on lithium tantalate substrates ( $42^\circ \text{LiTaO}_3$ ) and lithium niobate substrates ( $128^\circ \text{LiNbO}_3$ ) using electron beam evaporation technique. The films were investigated with respect to their texture using electron microscopy (SEM, TEM) and electron backscattered diffraction (EBSD). All layers were grown on a very thin titanium underlayer (thickness  $< 10 \text{ nm}$ ) to study the influence of titanium layer, substrate material and structuring on their texture development, power durability as well as lifetime. Experimental results show that the Ti interlayer and also the substrate material is essential to obtain an ideal strong (111)[110] texture without significant number of large angle grain boundaries. The fraction of the (111)[110] texture depends on the size of the metallization layer that indicates a correlation between texture and residual internal stress of the film. Consequently, SAW power durability and lifetime of fabricated power SAW test structures by using the lift-off technology is significantly enhanced in comparison to conventional Al fingers of a typical (111)-fibre texture.

**Cooperation** EPCOS AG, SAW Components Dresden, TU Dresden  
**Funded by** EPCOS

### Structure and properties of computer simulated ultralow- $k$ dielectrics for microelectronic application

H. Hermann, K. Zagorodniy, M. Taut

Classical and quantum-theoretical methods are used to design and to optimise insulating materials with extremely low static dielectric constant and reasonable mechanical properties. The hypothetical materials are generated as networks of cage-like molecules, e.g. fullerenes, which are interconnected by quasi-linear linker molecules. Structure optimisation, calculation of elastic moduli, and determination of the gap energy between highest occupied and lowest unoccupied molecular orbital (HOMO-LUMO gap) are carried out on a quantum-theoretical level while the static dielectric constant is estimated using the Clausius-Mossotti model. We varied the linker molecules and the topological arrangement of fullerenes in the network. The observed trends are: Replacement of hydrogen by fluorine in the linker molecules and transition from simple

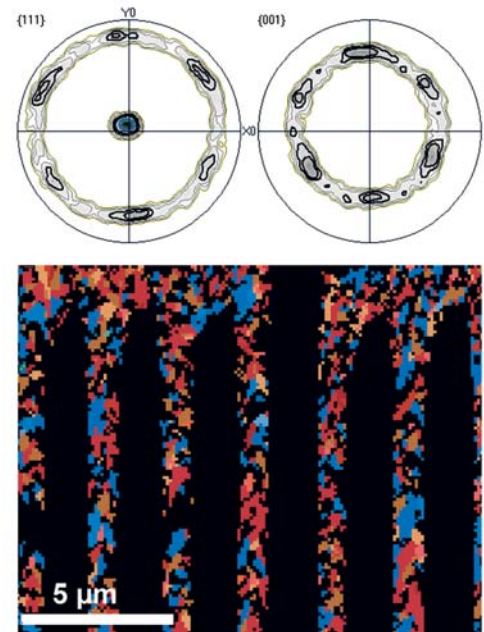


**Fig.:** EBSD results of a 192 nm thick aluminium layer on 5 nm titanium underlayer on  $42^\circ \text{LiTaO}_3$ ,  $1 \mu\text{m}$  finger structure of a 2 GHz filter device; strong texture, fraction of (111)[110]: fingers 66%; bond area 77%; blanket wafer 99...100%.

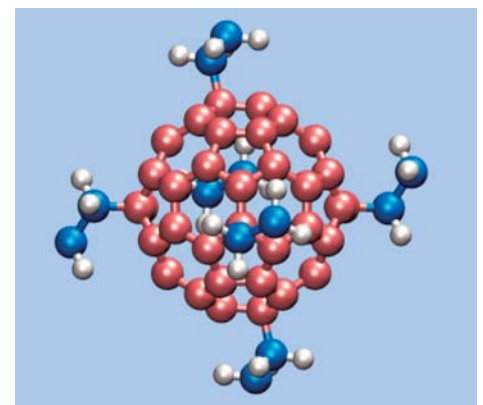


**Fig.:** Atomic structure of a  $\text{C}_{60}(\text{C}_2\text{H}_4)_6$  unit optimised for periodic boundary conditions. Big and small spheres represent carbon and hydrogen atoms, respectively.

cubic to diamond-like topology improve the relevant properties of the simulated materials. Diamond-like fullerene-based networks with Teflon-like linker molecules seem to be most promising as future ultralow- $k$  insulating materials for semi-conducting circuits [1]. Experimental verification is in progress [2].

[1] K. Zagorodny et al. *Phys. Rev. B* **75**, 245430 (2007).

[2] K. Zagorodny et al. *IEEE Transaction on Semiconductor Manufacturing* (submitted).

Cooperation AMD Saxony, TU Dresden, Univ. Wroclaw, BTU Cottbus

Funded by EU/SAB

### Co-Pt electrodeposition into nanoporous diblock copolymer templates

H. Schlörb, M. S. Khatri, S. Fähler, L. Schultz, S. Neitsch, K. Hennig

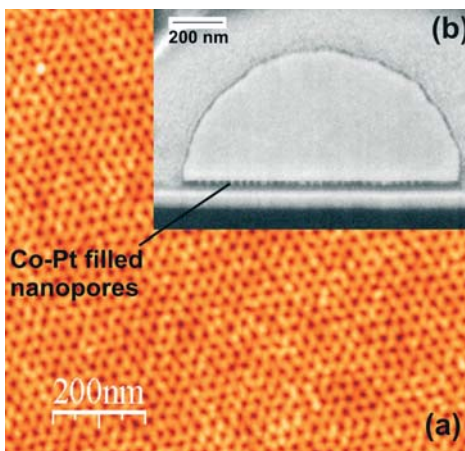


Fig.: AFM top view of a BC template (a) and FIB cross section after electrodeposition of Co-Pt (b).

Besides the  $L1_0$  phases of Fe-Pt and Co-Pt the Co rich phase near  $Co_{80}Pt_{20}$  is of high interest for future magnetic data storage media as it shows excellent hard magnetic properties and does not require thermal treatment to achieve them. Patterned media or even nanowires can be economically produced by electrodeposition into nanoporous templates. Following our experience on  $L1_0$  CoPt electrodeposition we have deposited Co-Pt films from an aqueous electrolyte containing cobalt sulphamate  $[Co(NH_2SO_3)_2]$  as the Co source and diamminedinitroplatinum  $[Pt(NH_3)_2(NO_2)_2]$  as the Pt source, respectively. It has been shown that the deposition current density strongly influences the magnetic properties whereas little changes in the film composition have been observed.

As nanoporous template we use diblock copolymer (BC) films as a promising alternative to aluminum oxide or polycarbonate membranes due to higher pore density and regular arrangement. Our templates consist of polystyrene-*b*-poly(4-vinylpyridine) with a pore diameter of  $\sim 8$  nm and an interpore distance of  $\sim 25$  nm which are hexagonally arranged after simple dip-coating and room temperature vapor annealing (fig. a). It was demonstrated that magnetic materials as Ni and Co-Pt (fig. b) can be successfully introduced into these nanopores by electrodeposition. Low wetting, swelling of the polymer, interactions between polymer and electrolyte as well as hydrogen evolution might be critical reasons for the non-uniform filling and thus are objects of further detailed investigations.

Cooperation IPF Dresden

Funded by DFG

### CNT-Copper Matrix Composite Films

S. Menzel, J. Thomas, T. Gemming, U. Weißker, F. Schäffel, S. Hampel, R. Kaltofen

Carbon nanotubes (CNTs) are of special interest not only for fundamental physical studies but also for materials research because they have outstanding mechanical, thermal, and electrical properties. Important breakthroughs have been reported in literature in recent years in the high-yield and structure-selective manufacturing and techniques for separating metallic and semiconducting CNTs, single or multiwall CNTs, or filling with different materials (e.g. Fe, Cu, Ni). The nm-size of such tubes makes commercial applications of this material as a reinforcing component in thin films possible. Large efforts due to chemical modification, manipulation and fabrication of CNTs allow the design and preparation of well-controlled architectures of such composite materials by incorporating tubes of special properties and in a well-defined orientation into appropriate matrices. It was already shown on powder-metallurgy processed material that such composites will have enhanced properties.

We are studying the preparation technique for CNT-copper matrix composite thin films of thickness in the  $\mu\text{m}$ -range. For this purpose CNTs were deposited onto a conducting underlayer system by a thermal CVD process. The conducting layer system consists of a barrier, a copper seed layer, and a dense Fe-particle arrangement as catalyst. After CNT deposition the copper films were grown by electroplating using a standard plating process with different additives. Furthermore, some experiments were carried out by adding the CNTs to the plating bath before deposition. Various pre-treatment steps for the carbon nanotubes were also investigated and discussed to improve copper adhesion at the CNT surface including formation of ultrathin Ta-based layers deposited by atomic layer deposition technique. Electron microscopy (SEM, TEM) and energy dispersive X-ray analysis (EDX) or energy filtered TEM show that a suitable wetting of copper on prepared CNT surface can be obtained and properties of fabricated composite films were investigated.

**Cooperation** TU Dresden, Fraunhofer-IKTS, FZ Dresden-Rossendorf

### Mn valence at Manganate/Titanate-Interfaces

T. Gemming, T. Riedl, K. Dörr, C. Thiele, L. Schultz, K. Wetzig

$\text{La}_{0.7}\text{Sr}_{0.3}\text{MnO}_3$  (LSMO) represents a promising material for applications in the field of magnetoelectronics. Its key properties comprise a high spin polarization of the charge carriers and a Curie point well above room temperature. Moreover, LSMO films grown on  $\text{SrTiO}_3$  (STO) substrate reach high crystal quality. LSMO/STO/LSMO tunnel junctions reveal huge magnetoresistance ratios at low temperature. However, the magnetoresistance of such junctions decreases rapidly with rising temperature, which is interpreted as a consequence of a deterioration of ferromagnetic order (i.e. electronic state of Mn) at the LSMO/STO interface. Electron energy-loss near edge fine structures (ELNES) in the scanning transmission electron microscope were used to probe the projected density of unoccupied states near the Fermi level at high lateral resolution at the interfaces.

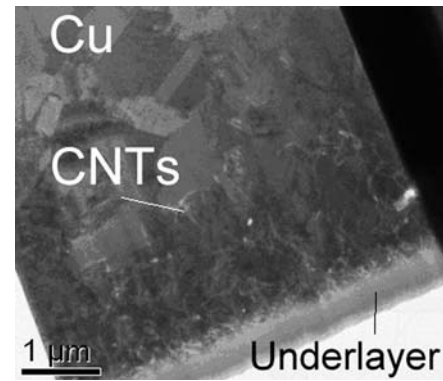
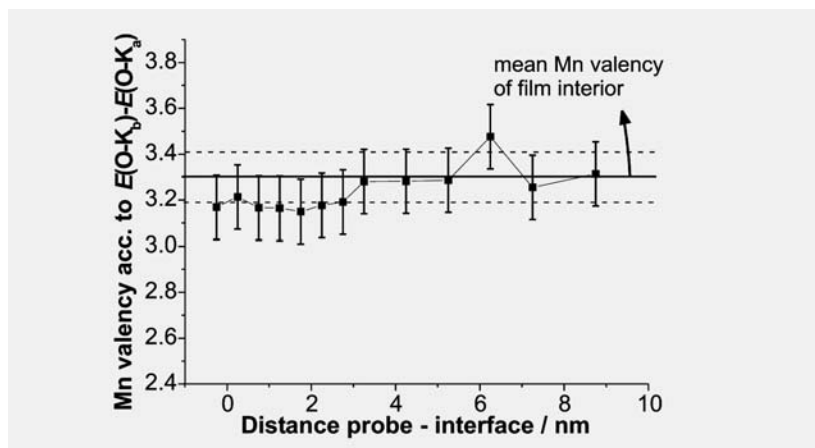


**Fig.:** TEM micrograph of a CNT-Cu matrix composite thin film on thermally oxidized Si(100) substrate. The length of the tubes grown on the substrate is some  $\mu\text{m}$ .

**Fig.:** Mn valency profiles at the interface between STO substrate and LSMO film according to the energy difference of subfeatures of the O-K edge  $|E(\text{O-K}_b) - E(\text{O-K}_a)|$ .

We found a reduction of the Mn valency at LSMO/STO (001) thin film interfaces, which can lead to a breakdown of ferromagnetic order. The detected Mn valency reduction of 0.1 - 0.2 compared to the film interior indicates a  $\text{La}_{0.7}\text{Sr}_{0.3}\text{O}/\text{TiO}_2$  atomic layer termination of the respective interfaces. Regarding the ELNES obtained in the STEM a second component with strongly varying intensity in interface-parallel direction occurs at the low energy-loss flank of  $\text{Mn-L}_3$ . It was shown that the LSMO/STO misfit and misorientation have a non-measurably small effect on the  $\text{Mn-L}_{2,3}$  ELNES. Therefore, oxygen vacancies are likely to provoke the  $\text{Mn-L}_3$  splitting.

Funded by DFG

### A new cell type of single phase unidirectional transducers for surface acoustic waves

S. Biryukov, G. Martin, B. Steiner (1) and B. Wall (1)

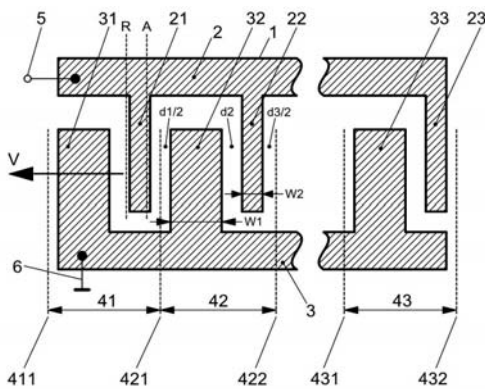


Fig.: Schematic view of a SPUDT including TF (two fingers) cells, V: direction of stronger SAW radiation.

Single phase unidirectional transducers (SPUDT) are essential components of surface acoustic wave (SAW) filters with low insertion loss and strong suppression of disturbing echo signals. Moreover, the internal reflections of the filters can be used for defined prolongation of the impulse response by means of them. By this, the same effects are achieved as by longer filter layouts. The basic elements of a SPUDT are called cells. DART (distributed acoustic reflection transducer) cells and Hunsinger cells consisting of three and four fingers, respectively, are the cell types used most frequently. For the first time, SPUDT cells including two fingers of different width only were found at IFW in 2007. Therefore, we call this cell type TF (two fingers) cell. It is constructed simpler than all the other SPUDT cell types known. Nevertheless, its unidirectional properties have not previously been found. As a consequence, a patent concerning devices including TF cells was submitted. The figure shows an embodiment of this invention. As given by the table, the reflection factor of TF cells on  $128^\circ\text{YX-LiNbO}_3$  is essentially larger than that of DART and Hunsinger cells in spite of a rather high coupling factor. As a result, especially short transducers can be realised.

cell type	finger number	coupling factor (%)	reflection factor (%)
TF	2	4.99	1.49
DART	3	3.05	0.72
Hunsinger	4	5.43	0.76

Cooperation Vectron International Telefilter, Teltow (1)

Funded by Vectron International Telefilter, Teltow